

Review

# Plasmonics Meets Perovskite Photovoltaics: Innovations and Challenges in Boosting Efficiency

Chen Wang<sup>1</sup>, Xiaodan Wang<sup>2</sup>, Bin Luo<sup>1</sup>, Xiaohao Shi<sup>1</sup> and Xiangqian Shen<sup>1,3,\*</sup>

<sup>1</sup> Xinjiang Key Laboratory of Solid State Physics and Devices, School of Physical Science and Technology, Xinjiang University, Urumqi 830046, China; w18336964902@163.com (C.W.); 107552303626@stu.xju.edu.cn (B.L.); 107552303638@stu.xju.edu.cn (X.S.)

<sup>2</sup> Department Interface Design, Helmholtz-Zentrum Berlin für Materialien und Energie GmbH (HZB), Albert-Einstein-Str. 15, 12489 Berlin, Germany; xiaodan.wang@helmholtz-berlin.de

<sup>3</sup> State Key Laboratory of Metal Matrix Composites, Shanghai Jiao Tong University, Shanghai 200240, China

\* Correspondence: sxqlyq@sjtu.edu.cn

**Abstract:** Perovskite solar cells (PSCs) have garnered immense attention in recent years due to their outstanding optoelectronic properties and cost-effective fabrication methods, establishing them as promising candidates for next-generation photovoltaic technologies. Among the diverse strategies aimed at enhancing the power conversion efficiency (PCE) of PSCs, the incorporation of plasmonic nanoparticles has emerged as a pioneering approach. This review summarizes the latest research advancements in the utilization of plasmonic nanoparticles to enhance the performance of PSCs. We delve into the fundamental principles of plasmonic resonance and its interaction with perovskite materials, highlighting how localized surface plasmons can effectively broaden light absorption, facilitate hot-electron transfer (HET), and optimize charge separation dynamics. Recent strategies, including the design of tailored metal nanoparticles (MNPs), gratings, and hybrid plasmonic–photonic architectures, are critically evaluated for their efficacy in enhancing light trapping, increasing photocurrent, and mitigating charge recombination. Additionally, this review addresses the challenges associated with the integration of plasmonic elements into PSCs, including issues of scalability, compatibility, and cost-effectiveness. Finally, the review provides insights into future research directions aimed at advancing the field, thereby paving the way for next-generation, high-performance perovskite-based photovoltaic technologies.



**Citation:** Wang, C.; Wang, X.; Luo, B.; Shi, X.; Shen, X. Plasmonics Meets Perovskite Photovoltaics: Innovations and Challenges in Boosting Efficiency.

*Molecules* **2024**, *29*, 5091. <https://doi.org/10.3390/molecules29215091>

Academic Editor: Terry Alford

Received: 12 September 2024

Revised: 18 October 2024

Accepted: 22 October 2024

Published: 28 October 2024



**Copyright:** © 2024 by the authors. Licensee MDPI, Basel, Switzerland. This article is an open access article distributed under the terms and conditions of the Creative Commons Attribution (CC BY) license (<https://creativecommons.org/licenses/by/4.0/>).

**Keywords:** perovskite solar cells; plasmonic nanoparticles; interface engineering; light harvesting; photovoltaic performance

## 1. Introduction

With the ongoing consumption of global energy and the escalating issues of environmental, the demand for green, clean, and renewable energy sources has become increasingly urgent. Among the various green energy options, solar energy is particularly notable due to their environmentally friendly, convenient utilization, and abundant availability [1–3]. Solar cells, which are pivotal devices for converting solar energy into electrical energy, play a crucial role in advancing the adoption of clean energy [4–11]. Perovskite Solar Cells (PSCs), as a pioneering class within thin-film photovoltaics, have garnered significant attention in recent years due to their remarkable progress in power conversion efficiency (PCE) [12–19]. Since their inception in 2009 with an initial PCE of 3.8%, PSCs have witnessed a meteoric rise, achieving a certified efficiency of over 26% in just a few years, surpassing many other emerging solar cell technologies [20–32]. This remarkable improvement can be attributed to their exceptional optoelectronic properties, such as high absorption coefficients, tunable bandgaps, and long carrier diffusion lengths [33–35]. However, despite these advantages, PSCs still face challenges related to their optical and electrical performance, particularly in terms of light absorption and charge transport, which limit their overall efficiency and

stability [36–41]. To this end, researchers have explored diverse strategies aimed at optimizing PSC performance, from improving material purity and stability to innovating device architectures and interfacial engineering [42–44].

One of the most promising avenues in this endeavor is the integration of plasmonic nanostructures into PSC designs. Plasmonic nanostructures represent an innovative class of materials that harness the unique optical properties of surface plasmons, the collective oscillations of electrons at the interface between a metal and a dielectric material [45–47]. These nanostructures can effectively manipulate light at the nanoscale, enabling precise control over light absorption, scattering, and confinement. The most commonly used materials for plasmonic nanostructures are metal nanoparticles (MNPs) with a high free electron density, particularly Au, Ag, and Al, due to their strong ability to support surface plasmons [48–50]. In addition to these, there are several other plasmonic materials, including metallic materials such as Mg, In, Na, and K; carbon-based materials like carbon nanotubes and graphene; metal alloy materials; semiconductor materials like indium–tin oxide (ITO), aluminum–zinc oxide (AZO), gallium–zinc oxide (GZO), GaAs, GaN, and GaP; as well as composite materials [51–57]. By tuning the size, shape, and composition of plasmonic nanostructures, researchers can engineer their optical resonances to match specific wavelengths, thus enhancing the interaction between light and matter in a desired manner [58–65]. In the context of PSCs, plasmonic nanostructures offer a promising solution by enhancing light absorption in the perovskite layer and facilitating efficient charge extraction. These structures can be categorized according to their placement within different layers, such as electron transport layer (ETL) [66], hole transport layer (HTL) [67], and perovskite active layers [68]. Figure 1 illustrates the strategies and enhancement mechanisms of plasmonic nanostructures in PSCs. Specifically, when integrated into PSCs, plasmonic nanoparticles, nanowires, or metasurfaces can concentrate and redirect incident sunlight into the active layer. The localized surface plasmon resonance (LSPR) of these nanostructures leads to significant absorption enhancements, particularly in the near-infrared and visible regions where the perovskite material might otherwise have limited absorption. This enhancement increases the overall photocurrent generation, a key parameter determining the efficiency of solar cells. Furthermore, plasmonic nanostructures can act as scattering centers, prolonging the optical path of light within the perovskite film, allowing for multiple absorption events. This scattering effect also contributes to a broader absorption spectrum and improved light harvesting efficiency. In addition to these optical enhancements, plasmonic nanostructures have also demonstrated their capability in improving the electrical performance of PSCs. For one thing, plasmon decay can generate hot electrons with energies exceeding the bandgap of the perovskite material. These hot electrons can be injected into the perovskite, contributing to the photocurrent and potentially bypassing some of the loss mechanisms associated with thermalization. For another, plasmonic nanostructures can also facilitate charge separation and transport processes within the solar cell by modifying the local electric field and providing additional pathways for charge carriers.

Given the significant progress made in the field, this review aims to provide a comprehensive overview of the latest research advancements in plasmonic nanostructures for enhancing the performance of PSCs. We will delve into the fundamental principles of surface plasmon polaritons (SPPs) and their excitation in various plasmonic nanostructures. Furthermore, we will examine the various strategies employed to integrate plasmonic nanostructures into PSC architectures, including nanoparticle embedding, nanohole arrays, and hybrid plasmonic–photonic designs. The optical and electrical enhancements achieved through these approaches, along with their underlying mechanisms, will be critically analyzed. Finally, we will discuss the remaining challenges and future directions for the continued advancement of plasmonic-enhanced PSCs.

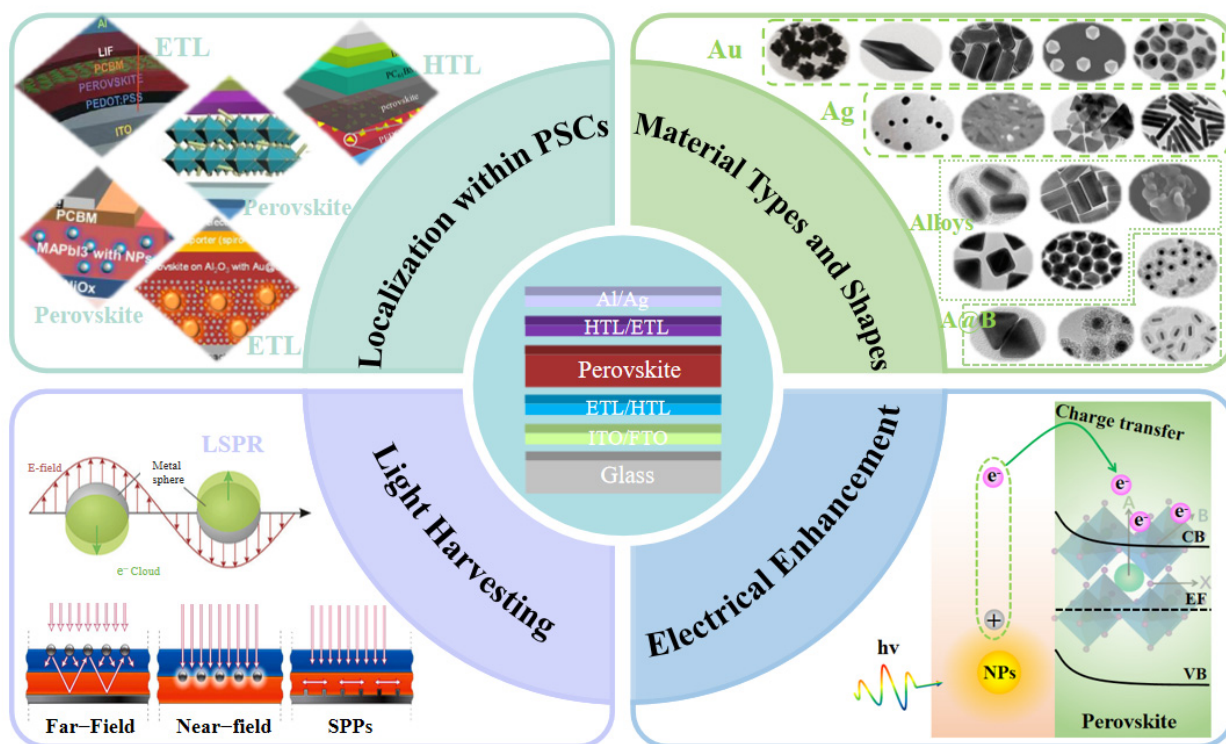


**Figure 1.** The strategies and enhancement mechanisms of plasmonic nanostructures in PSCs. Reproduced with permission from Ref. [69]. Copyright 2003, American Chemical Society. Reproduced with permission from Ref. [70]. Copyright 2010, Nature.

## 2. Mechanisms of Plasmonic Nanostructures for Enhanced Optical and Electrical Properties

When the light wave is incident on the interface between metal and dielectric, the free electrons on the metal surface undergo collective oscillations, coupling with the electromagnetic wave to form a near-field electromagnetic wave propagating along the metal surface [71]. If the oscillation frequency of the electrons is consistent with the frequency of the incident light wave, resonance will occur, forming LSPR. At this time, the energy of the electromagnetic field is effectively converted into the collective oscillation energy of the free electrons on the metal surface, thereby causing unique optical phenomena and enhancing the near-field electromagnetic field on or near the metal surface. Common metal materials mainly include Au, Ag, Al, Cu, etc., because these metals have relatively superior plasmonic properties and storage abundance in nature. The enhancement of solar cell performance by plasmonic metal nanostructures is mainly attributed to two modes, radiation effect and non-radiation effect [72]. The radiation effect includes far-field scattering and near-field coupling effects, while the non-radiation effect includes hot-electron transfer (HET) and plasmon resonance energy transfer (PRET). As shown in Figure 2, the working principles of these four enhancement mechanisms are discussed.

### 2.1. Far-Field Scattering

The essence of far-field scattering lies in the scattering of light onto metal nanostructures with high reflectivity, entering the far field. Depending on the geometric properties of particles and material properties, the scattering cross-section may be an order of magnitude larger than the physical cross-section of the nanostructure. Even at distances of hundreds of nanometers, this far-field-scattered light can still be reabsorbed by the light absorption layer in solar cells [73]. Photon scattering from nanostructures in the far field undergoes multiple scattering from proximal nanostructures, ultimately enhancing the total amount of light captured in solar cells. The optical scattering properties of different types of MNPs are influenced by various factors, including size, shape, composition, and dielectric envi-

ronment [74]. Therefore, we can adjust the LSPR to complement the wavelength range of the light absorption layer through carefully designed nanostructures, thereby achieving the reutilization of uncaptured photons and enhancing the light-harvesting efficiency of the device [75,76].

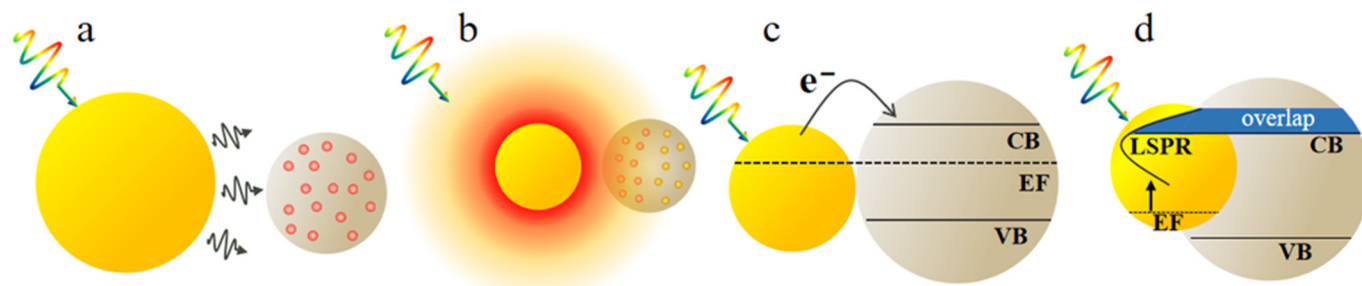


**Figure 2.** The four enhancement mechanisms of plasmonic nanostructures. (a) Far-field scattering. (b) Near-field coupling. (c) Hot-electron transfer. (d) Plasmon resonant energy transfer. Reproduced with permission from Ref. [72]. Copyright 2016, the Royal Society of Chemistry.

## 2.2. Near-Field Enhancement

When incident photons interact with plasmonic nanostructures and resonate, the electromagnetic field is confined within a small area on the metal surface and undergoes significant enhancement, known as near-field enhancement. In the direction perpendicular to the interface, the field strength of surface plasmons decays exponentially, but near the metal surface, its field strength is much higher than that of the incident light waves [77]. Surface plasmons have sub-wavelength localization, meaning their propagation is confined to a small region on the metal surface, leading to high energy concentration in the near-field region [78]. The enhancement effect mainly comes from the collective oscillation of free electrons on the metal surface, which binds and amplifies the electromagnetic waves. Strong near-field coupling effects occur around nanostructures, significantly enhancing the coupling between plasmas and molecules, thereby promoting the generation of electron-hole pairs in the active layer. Subsequently, these high-density charge carriers are effectively transferred to the  $\text{TiO}_2$ , thereby increasing the overall current density of the solar cell. Similar to far-field scattering, the near field generated by LSPR is also influenced by the shape and composition of the metal nanostructures. In particular, non-spherical nanostructures with sharp features generate high charge concentrations at the edges and corners, leading to slower decay of the generated near field, extending it further.

## 2.3. Hot-Electron Transfer

The non-radiative dissipation of plasmon energy can generate hot electrons through Landau damping, which possess higher energies than those produced by thermal excitation. Compared to electrons directly generated through interband transitions in semiconductors, hot electrons transferred from excited plasmonic metals exhibit a higher thermodynamic driving force and lower charge recombination for photocatalytic redox reactions [79,80]. The hot electrons generated by plasmons can directly interact with molecules adsorbed on the metal surface. Furthermore, the hot electrons can also be transferred to adjacent semiconductor supports via plasmon-mediated electron transfer pathways. In plasmonic metal/semiconductor systems, the excitation of plasmons significantly enhances the yield of hot electrons with high potential energy on the plasmonic metal and induces the rapid and efficient transfer of these hot electrons to the semiconductor [81]. The Schottky barrier aids in capturing the transferred hot electrons in the conduction band of the semiconductor by delaying the return of the hot electrons to the plasmonic metal. This plasmon-mediated electron transfer strategy effectively prolongs the lifetime of the hot electrons transferred to the semiconductor conduction band, thereby enabling them to promote various surface chemical reactions. To maximize the effectiveness of hot electron injection, close contact between the metal and semiconductor is essential [82,83]. There are numerous factors

influencing the generation and injection of hot electrons. Firstly, the size of the nanostructure plays a crucial role. Larger nanoparticles tend to produce hot carriers with very low excitation energies, whereas smaller metal particles often generate hot electrons that transition to higher energy levels. Additionally, smaller metal nanostructures favor the migration efficiency of hot electrons due to the limited migration speed of hot electrons in metals and their relatively short migration lifetime. It is estimated that the optimal size of gold nanoparticles ranges from 10 to 20 nm to maximize the generation and injection efficiency of hot electrons [84]. The second point concerns the shape of nanostructures. Theoretical calculations have shown that the hot electron injection rate of metallic nanorods is several orders of magnitude higher than that of spherical nanoparticles. With the aspect ratio remaining constant, the rate of hot electron injection into semiconductors increases as the aspect ratio of the nanorods increases but decreases as the volume of the nanorods increases. The third point pertains to the metal–semiconductor interface. Studies have indicated that the Schottky barrier height and defect states near the interface can impact the hot electron injection process. Strong near-field coupling at the plasmonic metal–semiconductor interface can facilitate hot electron transfer [85].

#### 2.4. Plasmon Resonant Energy Transfer

PRET is a novel energy transfer mechanism that relies on dipole–dipole interactions between noble metal MNPs and energy acceptor molecules to facilitate energy exchange. When the optical field generated by the LSPR of noble MNPs matches the excited state energy level of a semiconductor at a certain distance, non–radiative energy transfer from the donor to the acceptor is achieved through dipole–dipole interactions [86]. This energy transfer process does not involve the emission or absorption of photons but is realized directly through electric or magnetic field interactions. Compared to radiative energy transfer methods such as fluorescence resonance energy transfer (FRET), the PRET process does not involve the emission or absorption of photons, thereby reducing energy loss and background interference. Furthermore, the directions of energy transfer are fundamentally different between the two: in PRET, energy is transferred from the plasmon to the semiconductor, whereas in FRET, energy is transferred from the semiconductor to the plasmon. For HET, a minimum separation of 2 nm is required between the metal and the semiconductor, whereas PRET is not affected by any insulating interlayer. As long as the semiconductor is within the near-field range of the metallic nanostructure, an interaction between the LSPR and the semiconductor absorption occurs, leading to spectral overlap. Moreover, the occurrence of HET necessitates the alignment of the metal’s Fermi level with the semiconductor’s energy bands, whereas PRET is not constrained by Fermi level equilibration. The plasma enhancement of PSCs by PRET depends on the morphology and composition of the metal nanostructures as well as the distance between the semiconductor and the metal nanostructures [87].

### 3. Types of Plasmonic Materials in PSCs

#### 3.1. Noble Metal Plasmonic Nanomaterials

Noble metals Au and Ag are widely used to enhance the performance of PSCs due to their excellent plasmonic properties (resonance bands covering a broad range from visible to infrared regions of the solar spectrum). The local surface plasmon resonances of Au and Ag nanostructures are located near 520 nm and 400 nm, respectively, which can overlap with the absorption peaks of the active layer or ETL of solar cells, thereby promoting radiative and non-radiative coupling [77]. Although Au nanostructures exhibit visible band-to-band transitions and intraband transitions in the near-infrared (NIR) spectrum leading to high optical losses, their high stability, ease of synthesis, and direct visible light capture advantages still drive their application in PSCs [88,89]. Ag has low dielectric loss, determined by the imaginary part of the dielectric function [90,91], which results in Ag nanostructures having a higher extinction coefficient and greater light scattering [92,93], thereby increasing the light trapping efficiency of photovoltaic devices. The resonance

bands of both are mainly located in the visible light region, and the stable nature of the material itself make it possible to customize nanostructures with shapes and sizes that meet the requirements through physical or chemical methods, thereby effectively improving the photovoltaic performance of PSCs. The following will be classified according to the different shapes of Au, Ag, and their core–shell nanoparticles and a detailed summary and analysis of the application research progress and action mechanism of different metal nanostructures in PSCs.

### 3.1.1. Ag Nanomaterials

**Ag nanospheres.** Yang et al. investigated the effect of neatly arranged spherical Ag nanospheres added to the  $\text{TiO}_2$  photoanode layer of PSCs on the device's PCE [94]. The final results showed that a concentration of 0.5 wt% Ag nanospheres was optimal, which could achieve a PCE of 11.96% for the device. The intense plasmonic resonance response of Ag nanospheres enhanced a broad range of incident light absorption in the visible light wavelength region, improving charge transfer capability and beneficially enhancing the current density and photovoltaic conversion efficiency of PSCs. Meanwhile, the densely arranged Ag nanospheres on the  $\text{TiO}_2$  layer reduce its surface roughness and also contribute to the improvement of device performance. The schematic diagram, energy level diagram, and average thickness value of the device structure for PSCs are shown in Figure 3a.

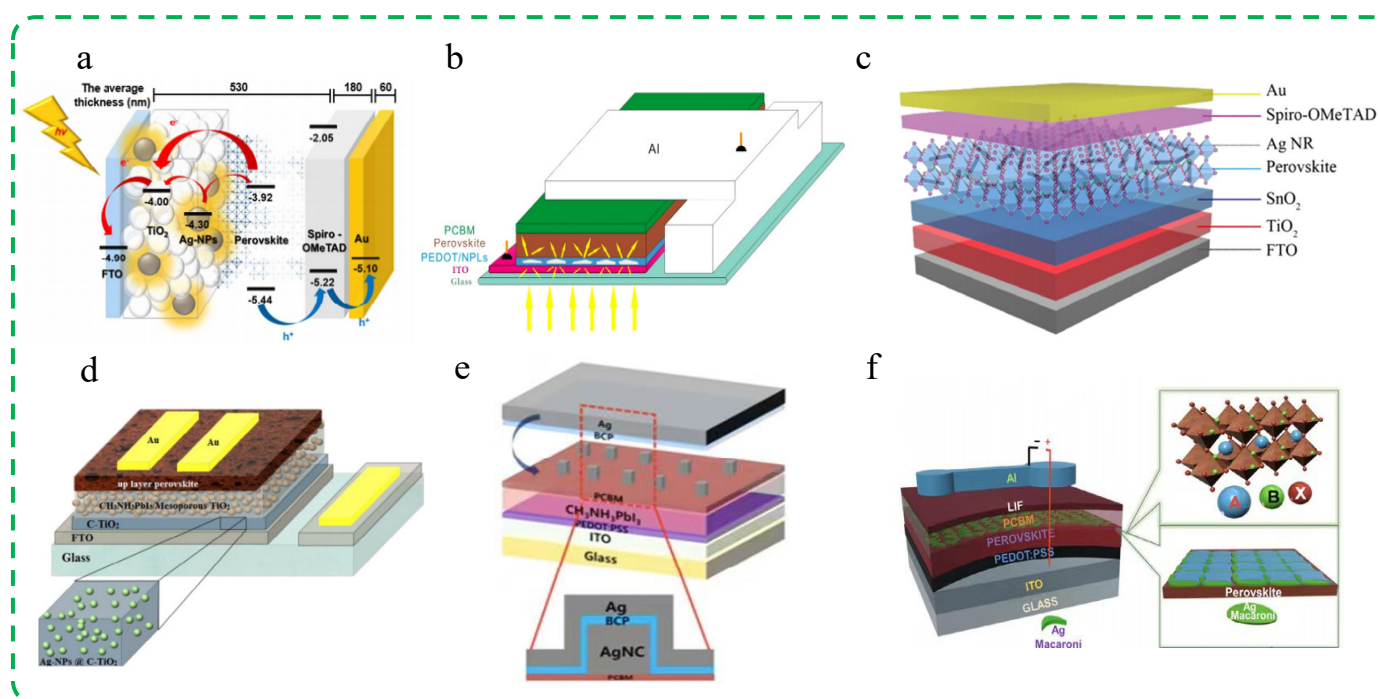


**Figure 3.** Summary of research for PSCs incorporating different Ag plasmonic nanostructures. (a) Ag nanospheres: Reproduced with permission from Ref. [94]. Copyright 2016, American Chemical Society. (b) Ag NPLs: Reproduced with permission from Ref. [95]. Copyright 2015, Elsevier. (c) Ag NRs: Reproduced with permission from Ref. [96]. Copyright 2020, Wiley. (d) Ag nanoparticles: Reproduced with permission from Ref. [97]. Copyright 2016, Elsevier. (e) Ag NCs: Reproduced with permission from Ref. [98]. Copyright 2017, American Chemical Society. (f) Ag NPLs: Reproduced with permission from Ref. [99]. Copyright 2020, Wiley.

**Ag nanoplates (NPLs).** Hsiang et al. adopted a wet chemical method to synthesize Ag NPLs with controllable shapes and sizes, with a thickness of  $12 \pm 4$  nm and a side length of  $70 \pm 20$  nm, supporting an SPR wavelength range of 500–750 nm [95]. With the increase in the edge length of Ag NPLs, the SPR band becomes broader, and the supported plasmonic effect also changes accordingly. By incorporating prepared Ag NPLs into the

HTL of PSCs, the device's PCE increased from the initial 8.5% to 9.6%, resulting in an overall improvement of 12.9%. This is attributed to the broad-band resonant absorption supported by the plasmonic Ag NPLs in the PSCs, leading to enhanced light harvesting of the photovoltaic device and thus improving efficiency. The schematic diagram of the PSCs device with Ag NPLs added is shown in Figure 3b.

Ag nanorods (NRs). Liu et al. introduced Ag NRs into the perovskite precursor solution by injecting the Ag NRs' water solution, thus incorporating the Ag NRs into the perovskite active layer [96]. The Ag NRs increase the light absorption cross-section and scattering cross-section through LSPR, ultimately increasing the probability of the perovskite layer capturing light, thereby enhancing the short-circuit current density ( $J_{SC}$ ) of the device. At the same time, the presence of appropriate water molecules helps to obtain high-quality larger grain size and less defective perovskite films, significantly increasing the fill factor (FF) of the device. The results show that Ag NRs have a good synergistic effect with water molecules, successfully reducing the defect density of the perovskite layer and significantly improving the mobility. When the added concentration reaches 2 vol%, the device performs best, with  $J_{SC}$  at 22.18 mA/cm<sup>2</sup>, FF at 81.68%, and PCE at 20.29%. Compared to the standard device without the addition of Ag NR solution, the performance parameters of the photovoltaic device have increased by 5.2%, 4.2%, and 9.7%, respectively. The device structure schematic diagram with the addition of Ag nanorod aqueous solution is shown in Figure 3c.

Ag nanoparticles. Precious MNPs can effectively enhance the light trapping efficiency of photovoltaic devices through the excitation of LSPR under illumination. Nouroulohi et al. embedded plasmonic Ag nanoparticles into the TiO<sub>2</sub> layer of mesoporous heterojunction PSCs to study their impact on the device's photovoltaic characteristics [97]. The final results showed that compared to samples without added Ag nanoparticles, the PCE of the fabricated cells increased by over 30%. According to the analysis of UV–visible absorbance data, the improved performance can be attributed to the far-field scattering and near-field coupling radiation effects of the Ag nanoparticles doped in the visible wavelength range of the solar spectrum, effectively extending the optical path of the incident light and increasing the photon absorption of the active perovskite layer. At the same time, the electron transfer time between the TiO<sub>2</sub> interface layer and the photovoltaic perovskite layer is reduced due to the improved frequency response of the electron transfer behavior in the photoelectric anode interface layer. The schematic diagram of the structure of the PSCs with added Ag nanoparticles is shown in Figure 3d.

Ag nanocubes (NCs). By enhancing the light absorption of the edge region of nanoparticles in plasmas, the PCE of high-efficiency solar cells can be further improved. Kim et al. have developed a planar PSCs with plasmonic Ag NCs electromagnetically coupled to a Ag back electrode, achieving the resonance wavelength control of the electrode-coupled plasmas [98]. By adjusting the thickness of the electron transfer layer inserted between the NCs and the electrode, the plasmon peak wavelength can be adjusted to the absorption edge of the perovskite active layer (600–800 nm). Due to the coupling with the Ag back electrode, the plasmonic resonance of Ag NCs is enhanced, leading to a significant improvement in far-field scattering and optical near-field originating from the nanocube faces closest to the perovskite layer. The electrode-coupled plasmon enhances the photocurrent at the edge of the PSCs, resulting in an increase in the average PCE from 11.9% to 13.3%. The schematic diagram of the PSC structure with electrode-coupled Ag NCs is shown in Figure 3e.

Ag NPLs. Ali et al. studied the effect of adding Ag NPLs based on vapor deposition to the perovskite active layer on device performance [99]. The final results show that the PCE of the device with Ag NPLs of size  $79 \pm 6$  nm added increased from 11.63% to 13.46%, with an improvement factor of 15.74%. In addition, the  $J_{SC}$  of the device also increased. Based on the LSPR effect, Ag NPLs exhibit the ability to enhance both near-field and far-field, scattering enhanced absorption and increasing the optical path length of photons in the active layer, effectively improving the photon–electron conversion efficiency of PSCs. In addition, the UV photoelectron spectroscopy shows a reduction in the hole injection barrier,

which also helps to improve the device performance. As shown in Figure 3f, a schematic diagram of a photovoltaic device structure containing Ag NPLs.

Ag@TiO<sub>2</sub>@Pa nanoparticles. Yao et al. added Ag@TiO<sub>2</sub>@Pa nanoparticles to the active layer of PSCs, improving light absorption and charge carrier extraction, ultimately resulting in increased  $J_{SC}$  and FF [100]. As shown in Figure 4(a1), a TEM image of the prepared nanoparticles, the size of the Ag@TiO<sub>2</sub>@Pa nanoparticles is 28 nm. With the synergistic effect of light effect and electrical effect, the addition of nanoparticles increases the efficiency of PSCs from 18.4% to 20.2%, an increase of 10.2%. As shown in Figure 4(a2,a3), the current density–voltage ( $J$ – $V$ ) curves and EQE spectra of the optimized reference device and plasma device are provided. The improvement in the efficiency of the photovoltaic device is attributed to the addition of core–shell nanoparticles, which reduce the losses when bare Ag nanoparticles are dispersed in the active layer; and it is also attributed to the field effect of LSPR and effective light scattering, increasing the generation of excitons and improving light absorption.

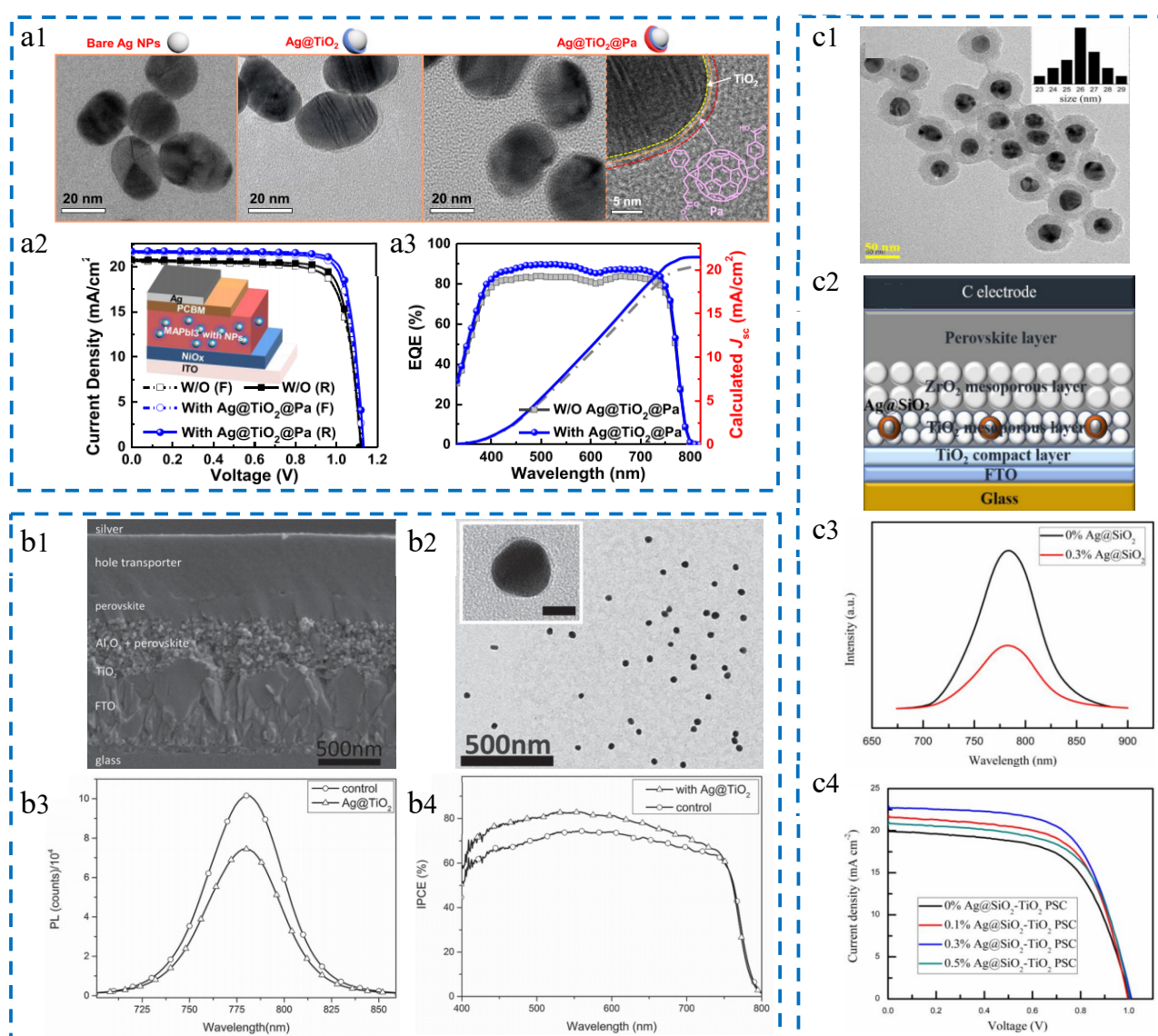


**Figure 4.** Summary of research for PSCs incorporating different Ag core–shell plasmonic nanostructures. (a1–a3) Ag@TiO<sub>2</sub>@Pa nanoparticles: Reproduced with permission from Ref. [100]. Copyright 2019, American Chemical Society. (b1–b4) Ag@TiO<sub>2</sub> nanoparticles: Reproduced with permission from Ref. [101]. Copyright 2015, Wiley. (c1–c4) Ag@SiO<sub>2</sub> nanoparticles: Reproduced with permission from Ref. [102]. Copyright 2018, MDPI.

Ag@TiO<sub>2</sub> nanoparticles. Michael et al. successfully incorporated core-shell Ag@TiO<sub>2</sub> nanoparticles into PSCs through a low-temperature processing approach, leading to an increase in device efficiency to 16.3% [101]. This enhancement is mainly attributed to the increase in  $J_{SC}$ . As shown in Figure 4(b1,b2), the scanning electron microscope (SEM) cross-section of the solar cell and the transmission electron microscope (TEM) image of Ag@TiO<sub>2</sub> nanoparticles, where the Ag@TiO<sub>2</sub> nanoparticles are composed of a 40 nm Ag core and a 2 nm TiO<sub>2</sub> shell, can be observed. Figure 4(b3,b4) separately represents the steady-state photoluminescence spectrum and the photovoltaic conversion efficiency of the reference device and the device with added Ag@TiO<sub>2</sub> nanoparticles. It can be seen from the figure that the addition of nanoparticles does improve the performance of the photovoltaic device, especially in the visible light range of 400–750 nm.

Ag@SiO<sub>2</sub> nanoparticles. Wang et al. synthesized Ag@SiO<sub>2</sub> nanoparticles using an improved oxidation method and integrated them into the mesoporous TiO<sub>2</sub> layer of PSCs [102]. This ultimately led to an increase in the PCE of the cell from 12.23% to 14.61% and an increase in  $J_{SC}$  from 20.23 mA/cm<sup>2</sup> to 23.04 mA/cm<sup>2</sup>. These enhancements are mainly attributed to the LSPR effect and strong scattering effect of Ag@SiO<sub>2</sub> nanoparticles. As shown in Figure 4(c1,c2), the TEM image and schematic structure of solar cells with Ag@SiO<sub>2</sub> nanoparticles are presented, where the size of the nanoparticles is 40 nm. Figure 4(c3) shows the photoluminescence spectrum of the device at room temperature, indicating that the addition of nanoparticles promotes the exciton ionization and charge separation processes. Figure 4(c4) displays the  $J$ - $V$  curves of the cells with different contents of Ag@SiO<sub>2</sub> nanoparticles added. It can be observed from the graph that the addition of nanoparticles is beneficial for improving the device performance, with the best effect achieved at a content of 0.3%.

### 3.1.2. Au Nanomaterials

Au nanostars (Au NSs). Wu et al. incorporated 40 nm Au NSs into the ETL of ultra-thin PSCs, enhancing light harvesting and charge carrier transport [103]. The schematic structure of the cell device is shown in Figure 5a. To prevent direct contact between Au NSs and the perovskite active layer, a TiO<sub>2</sub>/SnO<sub>2</sub> dual electron-modifying layer was introduced. In addition, the impact of Au NSs on the PCE of PSCs with different thicknesses was systematically studied, revealing varying improvements in PCE for different thicknesses of the perovskite layer with the introduction of the same Au NSs. For ultra-thin PSCs with a 250 nm perovskite layer, the PCE increased from 15.34% to 18.50%, with an enhancement factor of 20.60%; while for PSCs with a 400 nm perovskite layer, the PCE increased to 20.06%, with an enhancement factor of 13.70%.

Au nanorods (NRs). Gao et al. used the Asynchronous Synergistic Effect (ASE) strategy of water and Au NRs, adding a solution of Au NRs in water to the precursor solution of perovskite [104]. As shown in Figure 5b is the schematic structure of the cell device. The former improved the quality of the perovskite film during the crystallization process, reducing the defect density and increasing the carrier mobility. At the same time, when the device is exposed to light, the latter increases the light absorption of the perovskite layer through the LSPR effect. The results show that the ASE strategy has an excellent PCE of 21.73% and excellent long-term stability. After storing in air for 3 months, it can maintain 95% of the initial PCE.

Au nanoparticles. Lee et al. embedded Au nanoparticles into the HTL of PSCs to study the photovoltaic effect between PSC and Au nanoparticles [105]. Figure 5c shows the schematic structure of the cell device. The results show that Au nanoparticles cause near-field coupling in the short wavelength range, increasing  $J_{SC}$ . This is attributed to the LSPR effect and electron effect exhibited by Au nanoparticles. By comparing backscattered electron (BSE) data and atomic force microscope (AFM) images, it is shown that Au nanoparticles are located near the perovskite layer inside the HTL of PSCs. This implies that the improvement of EQE in PSCs by Au nanoparticles is a result of optical plasmonic effects and electronic contributions in a wide wavelength range.

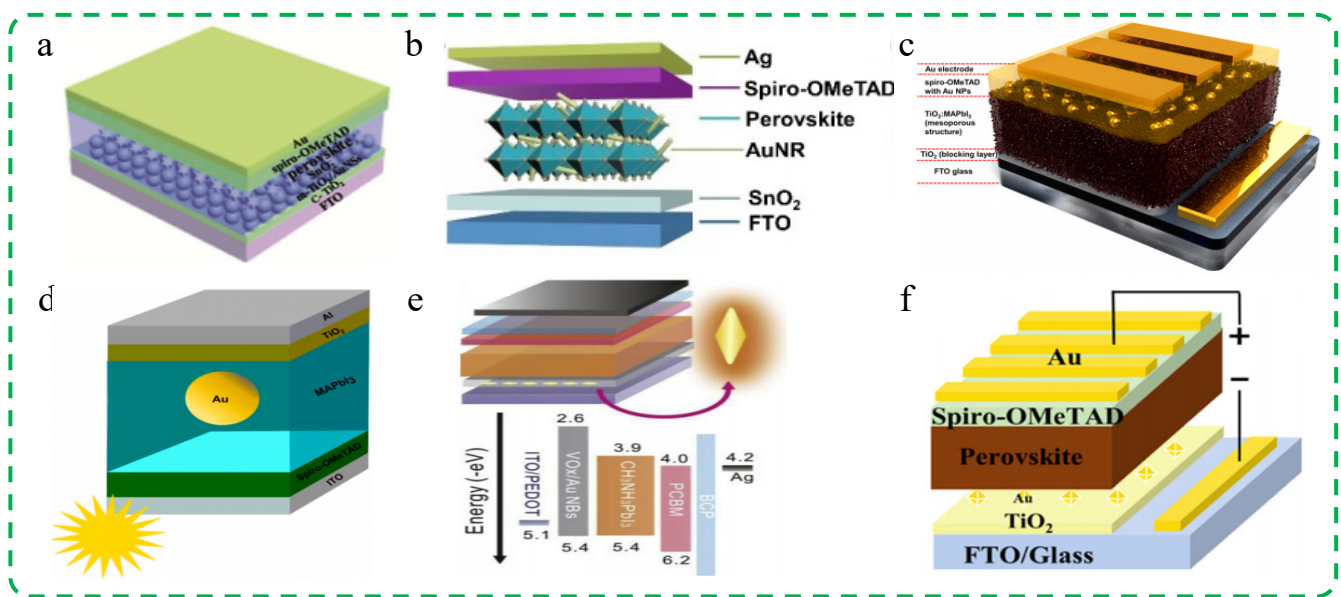


**Figure 5.** Summary of research for PSCs incorporating different Au plasmonic nanostructures. (a) Au NSs: Reproduced with permission from Ref. [103]. Copyright 2019, Elsevier. (b) Au NRs: Reproduced with permission from Ref. [104]. Copyright 2021, Wiley. (c) Au nanoparticles: Reproduced with permission from Ref. [105]. Copyright 2015, American Chemical Society. (d) Au nanosphere: Reproduced with permission from Ref. [106]. Copyright 2019, MDPI. (e) Au NBs: Reproduced with permission from Ref. [107]. Copyright 2018, Elsevier. (f) Au NOs: Reproduced with permission from Ref. [108]. Copyright 2021, American Chemical Society.

**Au nanosphere.** Elnaz and colleagues investigated the influence of adding spherical Au nanoparticles with different radii (20–60 nm) into the active layer of PSCs ( $\text{MAPbI}_3$ ) on their light absorption [106]. As shown in Figure 5d is the schematic structure of the cell device. It was found that the addition of 60 nm radius Au nanoparticles increased the light absorption of the cell by 20%. This is because placing plasmonic nanospheres in the device enhances the electric field around the nanoparticles, increasing the possibility of light absorption within the active layer. At the same time, both the amplitude and width of the absorbance spectrum of the PSCs were improved. As the radius of the nanoparticles increases, scattering is enhanced, leading to an overall increase in the cell's absorption.

**Au nanobipyramids (NBs).** Dong et al. prepared Au NB structure and incorporated it into the HTL of planar heterojunction PSCs, the schematic structure of the cell device is shown in Figure 5e [107]. This typical metallic nanostructure exhibits multiple and strong plasmonic absorption characteristics from visible light to NIR bands, showing a higher plasmon-induced probability. In addition, compared to traditional Au nanoparticles, the Au NBs show stronger electromagnetic field enhancement, thereby enhancing both light harvesting and improved interface charge dynamics. The final results show that the PCE of the best photovoltaic device with Au NBs is 18.84%, while the reference device's PCE is only 16.02%. At the same time, Au NBs also improve the electrical performance of the device. Under operating conditions, Au NBs effectively fill the hot hole injection, helping to increase the open circuit voltage, eliminate hysteresis effects, and improve long-term stability.

**Au nano-octahedrons (NOs).** Fang et al. synthesized Au NOs with broadband LSPR peaks and appropriate sizes and added them to the ETL ( $\text{TiO}_2$ ) of PSCs [108]. Figure 5f shows the schematic structure of the cell device. The results showed that the  $J_{SC}$  of the cell reached  $23.63 \text{ mA/cm}^2$ , and the PCE increased from 16.95% to 19.05%. This is because the LSPR of the nanostructure enhanced the light capture of the cell, improving the device's light harvesting capability and carrier extraction. Au NOs can enhance the light absorption of perovskite layers by increasing the light-scattering cross-section, and perovskite layers

can effectively excite more excitons. In addition, Au NOs also lower the surface potential of ETL, facilitating the extraction and transfer of electrons and holes photo-generated at the ETL/perovskite layer interface. Therefore, both  $J_{SC}$  and  $V_{OC}$  of PSCs have been significantly improved, leading to a corresponding enhancement in PSCs' efficiency.

**Au@SiO<sub>2</sub> nanoparticles.** Zhang et al. prepared Au@SiO<sub>2</sub> core-shell nanoparticles and integrated them into the ETL of PSCs [109]. The TEM image of the nanoparticles and the schematic structure of the cell device are shown in Figure 6(a1,a2). The final results show that the addition of Au@SiO<sub>2</sub> nanoparticles enhances the photocurrent and efficiency of the solar cells, reaching a device efficiency of 11.4%. The optimal performance  $J$ - $V$  curve of the battery is shown in Figure 6(a3). In contrast to other studies, the improved  $J_{SC}$  is attributed to the decrease in exciton binding energy, that is, the addition of MNPs enhances the generation of free charge carriers rather than enhancing light absorption.

**Au@SiO<sub>2</sub> nanoparticles.** The Au@SiO<sub>2</sub> nanoparticles prepared by Cui et al. are dispersed between two consecutive TiO<sub>2</sub> ETLs of PSCs [110]. This will result in the process of HET, where the hot electrons of the Au core can easily be injected into TiO<sub>2</sub>, thereby promoting the local electron migration of the TiO<sub>2</sub>, leading to improved charge transport and increased  $J_{SC}$ . At the same time, the HET effect rises to the Fermi level of TiO<sub>2</sub>, resulting in enhanced built-in potential and open-circuit voltage ( $V_{OC}$ ). Finally, efficiencies of 18.81% and 19.42% were achieved in planar and mesoscopic structure PSCs, respectively. Figure 6(b1) shows the TEM image of Au@SiO<sub>2</sub> core-shell nanoparticles, revealing a nanoparticle size of 18 nm. Figure 6(b2) depicts the structure of the PSCs. Figure 6(b3) UV-visible absorption and time-integrated PL spectra indicate a significant decrease in PL due to the addition of nanoparticles, suggesting charge transfer from perovskite to TiO<sub>2</sub>.

**Au@CdS nanoparticles.** Qin et al. synthesized core-shell Au@CdS nanospheres, dispersed between the active layer and the HTL of PSCs, with a nanoparticle size of 35 nm [111]. Figure 6(c1,c2) show the high-resolution transmission electron microscope (HR-TEM) image of the nanospheres and the structural diagram of the PSC device, respectively. With the LSPR effect of Au@CdS, holes can easily overcome barriers at the perovskite interface, avoid carrier accumulation, suppress carrier trap recombination at the Spiro-OMeTAD/perovskite interface, effectively improve the generation/dissociation of excitons, and promote the transfer/collection of carriers. Therefore, the PSC device based on Au@CdS achieved an efficiency of over 21%.

**Au@PSS nanoparticles.** Hao et al. incorporated Au@PSS nanoparticles prepared into PSCs to enhance the light absorption of lead iodide (PbI<sub>2</sub>) through the surface plasmon resonance effect [112]. The use of tetrahedral Au cores and the introduction of ultra-thin PSS shell layers are both beneficial for generating a strong localized field and preventing exciton quenching on the surface of the nanoparticles. At the optimal concentration of Au@PSS nanoparticles, the PCE reached 16.53%, with a significant enhancement factor of 18.83% compared to the reference device without nanoparticles. The results indicate that in addition to promoting light absorption in the active layer, Au@PSS nanoparticles also enhance the composite resistance inside PSCs and improve exciton dissociation and charge transfer efficiency by reducing the intensity of photoluminescence and the lifetime of excitons/carriers.

In addition to the noble metal geometrical shapes discussed in the above figures, we also provide a comprehensive list in Table 1, including a range of shape-controlled noble metal and their core-shell nanostructures that have recently been used in PSCs in the literature. This provides a reference for further exploring the working mechanism of noble metal plasmonic nanostructures, enhancing PSCs, and further perfecting the theoretical system of the application of LSPR effects in PSCs.

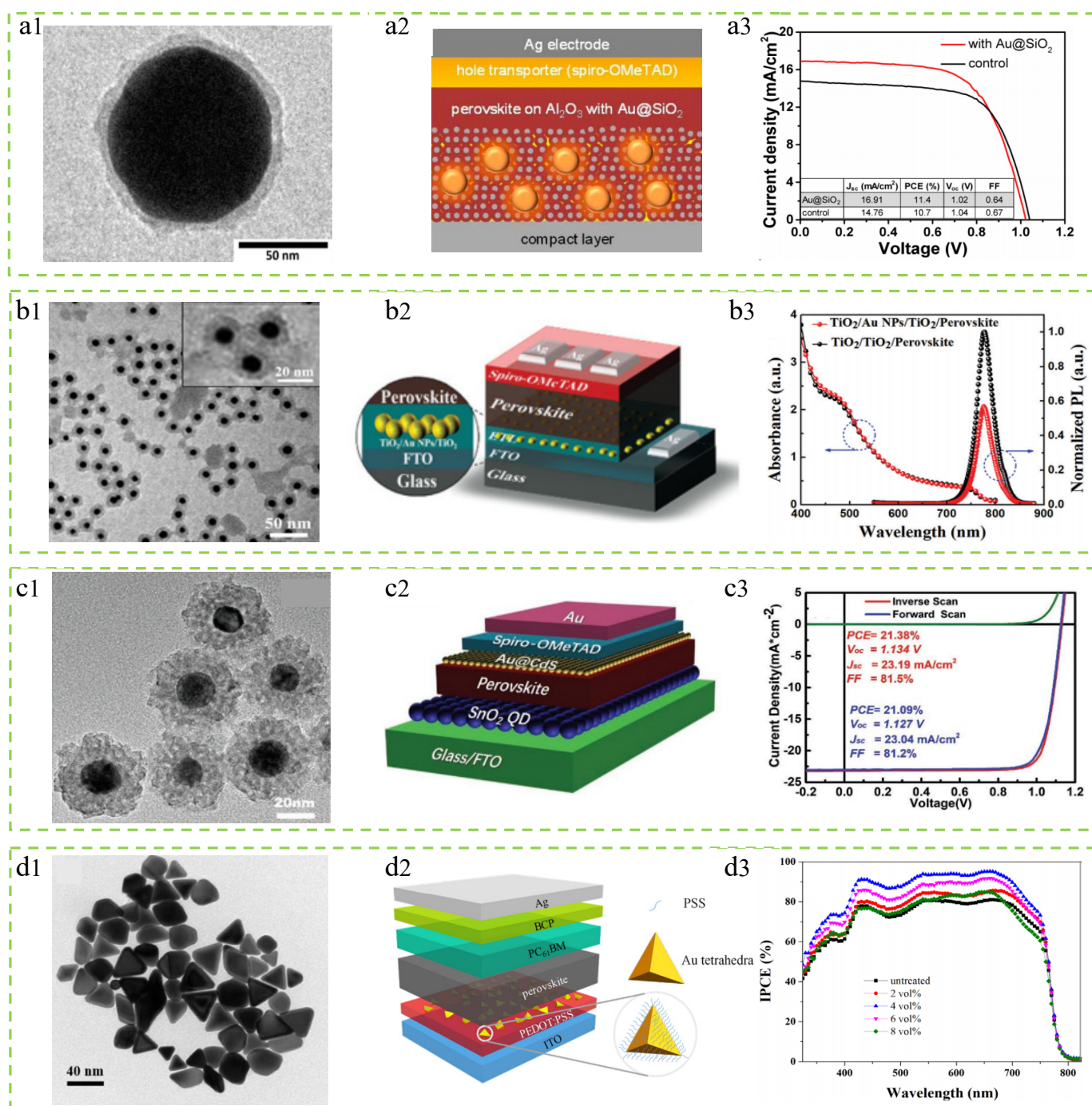


**Figure 6.** Summary of research for PSCs incorporating different Au core-shell plasmonic nanostructures. (a1–a3) Au@SiO<sub>2</sub> nanoparticles: Reproduced with permission from Ref. [109]. Copyright 2013, American Chemical Society. (b1–b3) Au@SiO<sub>2</sub> nanoparticles: Reproduced with permission from Ref. [110]. Copyright 2020, the Royal Society of Chemistry. (c1–c3) Au@CdS nanoparticles: Reproduced with permission from Ref. [111]. Copyright 2020, Wiley. (d1–d3) Au@PSS nanoparticles: Reproduced with permission from Ref. [112]. Copyright 2018, Wiley.

**Table 1.** Summary of photovoltaic parameters for PSCs incorporating noble metal and their core-shell plasmonic nanomaterials. (The numbers in parentheses indicate the reference device performance.)

| Materials               | Size                              | Position of NPs  | $J_{SC}$ (mA/cm <sup>2</sup> ) | $V_{OC}$ (V)  | FF (%)        | $\Delta FF$ (%) | PCE (%)       | $\Delta PCE$ (%) | Ref   |
|-------------------------|-----------------------------------|--|--------------------------------|---------------|---------------|-----------------|---------------|------------------|-------|
| Ag nanoparticles        | 25 nm                             | ETL (TiO <sub>2</sub> )                                  | 18.91 (17.85)                  | 0.90 (0.88)   | 70.20 (69.46) | 1.07            | 11.96 (10.96) | 9.12             | [94]  |
| Ag nanomaterials        | 10–100 nm                         | ETL  | 1.13 (1.05)                    | 24.51 (24.67) | 80.93 (75.13) | 7.72            | 22.42 (19.52) | 14.86            | [113] |
| Ag NPLs                 | 70 ± 20 nm                        | HTL (PEDOT: PSS)   | 15.40 (13.70)                  | 0.92 (0.88)   | 68.20 (70.70) | −3.54           | 9.60 (8.50)   | 12.94            | [95]  |
| Ag NRs                  | 20 nm (200 nm)                    | Perovskite   | 22.18 (21.08)                  | 1.12 (1.12)   | 81.68 (78.36) | 4.24            | 20.29 (18.50) | 9.68             | [96]  |
| Ag nanoparticles        | 30 nm                             | ETL (TiO <sub>2</sub> )                                  | 13.14 (10.96)                  | 0.78 (0.72)   | 60.18 (58.42) | 3.01            | 6.15 (4.57)   | 34.57            | [97]  |
| Ag NCs                  | 70 nm                             | ETL (PCBM)   | 21.40 (19.50)                  | 1.00 (1.00)   | 62.00 (61.00) | 1.64            | 13.30 (11.86) | 12.14            | [98]  |
| Ag NPLs                 | 79 ± 6 nm                         | Perovskite   | 24.41 (19.89)                  | 0.85 (0.90)   | 65.00 (65.00) | 0.00            | 13.46 (11.63) | 15.74            | [99]  |
| Ag@TFP NPs              | 10–15 nm                          | Between perovskite and HTL                               | 24.79 (23.52)                  | 1.19 (1.15)   | 80.44 (78.96) | 1.87            | 23.86 (21.54) | 10.77            | [114] |
| Ag@TiO <sub>2</sub> @Pa | 28 nm                             | MAPbI <sub>3</sub>                                       | 21.69 (20.71)                  | 1.13 (1.12)   | 83.00 (79.00) | 5.06            | 20.24 (18.37) | 10.18            | [100] |
| Ag@TiO <sub>2</sub>     | 42 nm                             | ETL  | 22.00 (20.20)                  | 1.06 (1.03)   | 69.00 (67.00) | 2.99            | 16.30 (14.50) | 12.41            | [101] |
| Ag@SiO <sub>2</sub>     | 40 nm                             | ETL (TiO <sub>2</sub> )                                  | 23.04 (20.23)                  | 1.02 (1.00)   | 62.17 (60.45) | 2.85            | 14.61 (12.23) | 19.46            | [102] |
| Ag@SiO <sub>2</sub>     | 50 nm                             | HTL (PEDOT: PSS)   | 22.58 (20.21)                  | 1.01 (0.97)   | 75.50 (74.40) | 1.48            | 17.22 (14.58) | 18.11            | [115] |
| Au NRs                  | 104.8 ± 6.8 nm<br>(37.4 ± 1.8 nm) | Between perovskite and HTL                               | 24.82 (22.88)                  | 1.09 (1.08)   | 81.18 (80.47) | 0.88            | 22.02 (19.96) | 10.32            | [64]  |
| Au NRs                  | 50 nm (20 nm)                     | Perovskite   | 21.60 (21.03)                  | 1.10 (1.09)   | 81.92 (78.65) | 4.16            | 19.46 (18.02) | 7.99             | [116] |
| Au NSs                  | 40 nm                             | ETL(TiO <sub>2</sub> )                                   | 22.30 (20.97)                  | 1.13 (1.11)   | 80.00 (76.00) | 5.26            | 20.06 (17.64) | 13.72            | [103] |
| Au NRs                  | 17 nm (93 nm)                     | Perovskite   | 23.72 (22.98)                  | 1.11 (1.11)   | 82.47 (78.48) | 5.08            | 21.73 (20.12) | 8.00             | [104] |
| Au nanoparticles        | 15 nm                             | HTL (Spiro-OMeTAD)                                       | 20.04 (19.63)                  | 0.95 (0.96)   | 66.96 (67.23) | −0.40           | 12.74 (12.66) | 0.63             | [105] |
| Au NBs                  | 45–50 nm<br>(15–18 nm)            | HTL(VOx)   | 22.68 (—)                      | 1.08 (—)      | 77.10 (—)     | —               | 18.84 (16.02) | 17.60            | [107] |
| Au NOs                  | 115 nm                            | ETL(TiO <sub>2</sub> )                                   | 23.63 (22.29)                  | 1.08 (1.05)   | 73.90 (72.38) | 2.10            | 19.05 (16.95) | 12.39            | [108] |
| Au@SiO <sub>2</sub> NPs | 80 nm                             | ETL  | 16.91 (14.76)                  | 1.02 (1.04)   | 64.00 (67.00) | −4.48           | 11.40 (10.70) | 6.54             | [109] |
| Au@SiO <sub>2</sub> NPs | 18 nm                             | ETL  | 22.30 (20.90)                  | 1.07 (1.04)   | 72.12 (—)     | —               | 19.42 (17.76) | 9.35             | [110] |
| Au@CdS NPs              | 35 nm                             | Between perovskite and HTL                               | 23.14 (21.40)                  | 1.12 (1.09)   | 79.90 (75.60) | 5.69            | 20.67 (17.71) | 16.71            | [111] |
| Au@PSS NPs              | 54 nm                             | HTL (PEDOT: PSS)   | 23.34 (20.41)                  | 1.06 (1.07)   | 70.50 (67.30) | 4.75            | 16.53 (13.91) | 18.84            | [112] |
| Au@GO NPs               | 28 nm                             | Between perovskite and HTL (PEDOT: PSS)                  | 18.56 (17.05)                  | 1.02 (0.99)   | 74.00 (72.00) | 2.78            | 14.00 (12.17) | 15.04            | [117] |
| Au@SiO <sub>2</sub> NPs | −25 nm                            | HTL (NiO)  | 20.86 (20.40)                  | 1.12 (1.12)   | 79.28 (79.72) | −0.55           | 18.52 (18.21) | 1.70             | [118] |
| Au@NiO NPs              | −25 nm                            | HTL (NiO)  | 21.75 (20.40)                  | 1.15 (1.12)   | 82.42 (79.72) | 3.39            | 20.61 (18.21) | 13.18            | [118] |
| Au@SiO <sub>2</sub> NPs | 14 nm                             | ETL (between c-TiO <sub>2</sub> and m-TiO <sub>2</sub> ) | 20.73 (19.86)                  | 1.08 (1.08)   | 78.29 (75.71) | 3.41            | 17.55 (16.18) | 8.47             | [119] |
| Au@TiO <sub>2</sub> NPs | 80 nm                             | Between porous TiO <sub>2</sub> and MAPbI <sub>3</sub>   | 23.12 (17.40)                  | 1.04 (0.98)   | 75.50 (73.70) | 2.44            | 18.24 (12.59) | 44.88            | [120] |
| Au@TiO <sub>2</sub> NPs | 70 nm                             | Perovskite   | 22.93 (18.70)                  | 0.97 (0.93)   | 83.30 (82.28) | 1.24            | 18.47 (14.32) | 28.98            | [121] |

### 3.2. Other Metal Plasmonic Nanomaterials

#### 3.2.1. Al Nanomaterials

In addition to precious metals such as Au and Ag, Al is recommended as a new alternative plasma material due to its advantages of low cost, abundant natural reserves, and broad response range in plasma spectroscopy [122,123]. It has a plasma frequency of up to about 15.3 eV, much higher than Ag's 9.6 eV and Au's 8.55 eV [124], so it can extend the surface plasma response to the ultraviolet region and support long-lived LSPR with high optical cross-section. Meanwhile, unlike Au and Ag, the work function of Al (4.06 eV) is lower than that of TiO<sub>2</sub> (4.26 eV), so using Al significantly reduces the expected quenching through charge transfer and carrier recombination, effectively improving the extraction efficiency of charge carriers. Additionally, due to low light loss and minimal plasmon damping, Al nanoparticles have higher light-scattering efficiency in visible light compared to Au and Ag [125]. In addition, a thin layer of natural oxide formed on the surface of Al can prevent further oxidation and contamination inside, thus ensuring the stability of the material itself. At the same time, it can avoid direct contact between the Al metal itself and the active layer and ETL of solar cells, reducing the generation of harmful radiation. Arul et al. increased the PCE of the device by 14% by placing Al nanoparticles with particle sizes ranging from 20 to 70 nm between the ETL and the electrode [126]. The addition of Al nanoparticles exhibited a dual effect, namely, local surface plasmon resonance and far-field scattering, thereby improving photon absorption in the active layer and increasing the photovoltaic conversion efficiency of PSCs. At the same time, the electrical conductivity and  $J_{SC}$  of the device have also been improved. It is also observed that the presence of Al nanoparticles in the ETL slightly reduces the deep trap density, while there is no change in the shallow trap state, thereby increasing the carrier concentration of the device.

#### 3.2.2. Cu Nanomaterials

Similar to the advantages of Al materials, Cu is also one of the materials that receive considerable attention besides noble metals such as Au and Ag. On the one hand, this is because of its low material cost, and, on the other hand, it displays good plasma characteristics in the visible light wavelength region, possessing photovoltaic properties similar to Au and Ag. If Cu nanoparticles can be successfully used to enhance the efficiency of PSCs, it can reduce manufacturing costs while maintaining the light absorption of solar cells, thereby promoting the development of solar cells and achieving commercial production sooner. Shreya et al. simulated the effect of adding Cu nanoparticles to PSCs using the Finite Difference Time Domain (FDTD) method and conducted a rigorous analysis of the size and position of the nanoparticles [127]. It was ultimately found that adding spherical nanoparticles with a radius of 70 nm at the center of the 200 nm perovskite layer can achieve the maximum enhancement effect.

### 3.3. Alloy Plasmonic Nanomaterials

Apart from size and morphology, the composition also affects the LSPR properties of plasma nanoparticles. In order to prepare nanoparticles that meet the requirements, researchers have designed composite structures of dual materials, with the most typical being Au-Ag alloy nanostructures. It is well known that Au and Ag nanoparticles themselves have strong plasmonic properties, so the coupling effect of the two materials will lead to a further enhancement of the plasmon resonance mode [128,129], characterized by an increase in the number of LSPR extinction peaks. Compared to single MNPs, alloy nanoparticles have greatly improved absorption and scattering intensities and broader and stronger plasmon resonance effects, ultimately achieving enhanced broadband absorption [130]. In addition, due to the strong coupling between the two metals, the intensity of the near-field electromagnetic field of alloy nanoparticle LSPR is significantly increased [131], which can reduce the number of MNPs used in plasmonic solar cells, thereby improving material utilization and reducing production costs. Therefore, alloy nanoparticles are of great significance for enhancing the performance of plasmonic PSCs.

Au@Ag nanocuboids. Fu et al. synthesized Au@Ag-alloy-encapsulated nanocuboids. Compared to traditional metal nanostructures with a single narrow plasmon resonance band, Au@Ag nanoparticles exhibit multiple broader and stronger plasmon resonances [132]. By adjusting the structural size to match the spectral absorption band of perovskite, especially in its weak absorption region. By adjusting the position of Au@Ag nanoparticles in the electrode, the performance of PSCs can be effectively improved by utilizing the plasmonic near-field enhancement and increased light-scattering effects. Figure 7(a1,a2) show the TEM images of Au@Ag core-shell nanocuboids and the cross-sectional SEM image of PSCs with added Au@Ag core-shell nanocuboids, respectively. Figure 7(a3,a4) represent the statistically averaged PCE of the devices and the parameter curves of the best-performing device. It can be observed that the device's PCE is concentrated around 17.5%, while the champion PCE of the best plasmonic PSCs is 18.31%.

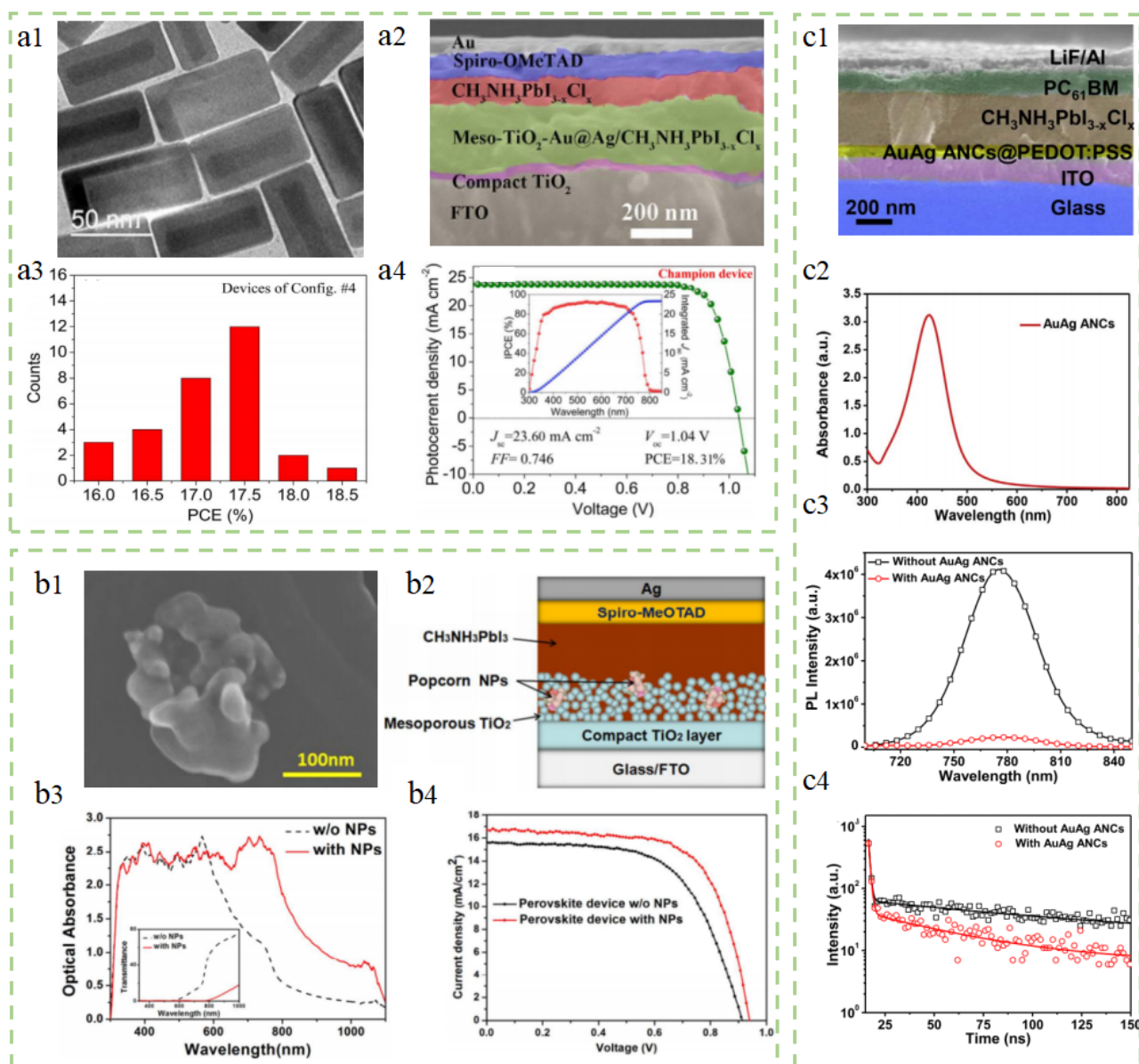


**Figure 7.** Summary of research for PSCs incorporating different alloy nanomaterials. (a1–a4) Au@Ag nanocuboids: Reproduced with permission from Ref. [132]. Copyright 2017, Elsevier. (b1–b4) Au–Ag alloy popcorn-shaped nanoparticles: Reproduced with permission from Ref. [133]. Copyright 2012, the Royal Society of Chemistry. (c1–c4) AuAg alloy nanocrystals: Reproduced with permission from Ref. [134]. Copyright 2017, Elsevier.

Au-Ag alloy popcorn-shaped nanoparticles. Lu et al. prepared Au-Ag alloy popcorn-shaped nanoparticles and placed them in the ETL of PSCs [133]. The TEM image of the popcorn-shaped nanoparticles is shown in Figure 7(b1), with an average size of  $150 \pm 50$  nm. The unique popcorn nanoparticles have the advantage of exciting various LSPR modes in a broader range of solar spectral. As shown in Figure 7(b3,b4), the optical absorption curve with added nanostructures and the  $J$ - $V$  curve of the best-performing perovskite device are presented. It can be observed from the figures that the addition of popcorn-shaped nanoparticles not only broadens the device's absorption spectrum of solar light but also effectively improves the  $J_{SC}$  of the device. Therefore, by using these nanoparticles, the light absorption of PSCs can be significantly enhanced, and the photoinduced charge transfer can be improved. As a result, the maximum PCE of the device increased from 8.9% to 10.3%, representing a 15.7% increase.

AuAg alloy nanocrystals. Sun et al. synthesized AuAg core-shell alloy nanocrystals (ANCs) with a size of 46 nm, doped into the HTL (PEDOT: PSS) of PSCs [134]. Figure 7(c2) shows a cross-sectional SEM image of the device with added nanoparticles. Figure 7(c1) shows the UV-visible absorption spectrum of AuAg ANCs, displaying a dense characteristic absorption peak at 428 nm. Figure 7(c3,c4) show steady-state and time-resolved PL spectra of perovskite films with and without AuAg alloy nanoparticles on the PEDOT: PSS layer. The image shows that the perovskite film with added nanoparticles exhibits a significant PL quenching, indicating enhanced charge transfer from the perovskite film to the HTL. Ultimately, the device doped with nanoparticles achieved a champion PCE of 16.76%, a 28% increase compared to the undoped device (13.14%). The study shows that the significant improvement in device performance is primarily attributed to the scattering effect of AuAg alloy nanocrystals that improve light collection and optimize charge transfer in the HTL.

### 3.4. Other Novel Plasmonic Nanomaterials

AuAgNPrisms@SiO<sub>2</sub>. Han et al. successfully prepared SiO<sub>2</sub>-coated AuAg-alloyed nanoprisms and evenly distributed them between the HTL and active layer of inverted PSCs [135]. The final results show that the best-performing device has  $J_{SC}$  and PCE of 7.08 mA/cm<sup>2</sup> and 4.60%, respectively, which are 32.8% and 34.1% higher than the control group ( $J_{SC} = 5.33$  mA/cm<sup>2</sup> and 3.43%). As shown in Figure 8(a3,a4), the  $J$ - $V$  curves and external quantum efficiency (EQE) curves with different concentrations of AuAgNPrisms@SiO<sub>2</sub> nanoparticles are presented. It can be observed from the figures that the addition of nanoparticles significantly increases  $J_{SC}$  while slightly decreasing the  $V_{OC}$ . Among the devices with three doping concentrations, the device with a concentration of 0.7 mM/mL performs the best. Meanwhile, the addition of AuAgNPrisms@SiO<sub>2</sub> nanoparticles reduces the series resistance ( $R_s$ ), leading to a significant increase in FF. The enhancements in  $J_{SC}$  and FF outweigh the decrease in  $V_{OC}$ , resulting in an increased PCE of PSCs. In addition, the added AuAgNPrisms@SiO<sub>2</sub> nanoparticles can act as inducers to enhance the smoothness of the perovskite film, increase light absorption, promote exciton dissociation, and facilitate charge carrier transport.

Si nanoparticles. Aleksandra et al. studied the effect of adding resonant Si nanoparticles between the TiO<sub>2</sub> transport layer and the active layer on the performance of PSCs [136]. Figure 8(b1,b2) show the band diagram and cross-sectional bright-field STEM image of the PSCs, where the size of the added silicon nanoparticles is 140 nm. Figure 8(b3,b4) show the efficiency and  $J_{SC}$  data of the photovoltaic devices. According to the data in the figure, it can be seen that the PCE of all devices is above 15%, with the highest PCE of the optimal device being 18.8%. Compared with batteries without added nanoparticles, the presence of Si nanoparticles significantly improves the average  $J_{SC}$  and optimal  $J_{SC}$  of the batteries. The final research results show that the photocurrent and FF of PSCs have also been enhanced, reaching 22.4 mA/cm<sup>2</sup> and 78.9% respectively. This is attributed to the plasmonic effect exhibited by Si nanoparticles, which leads to near-field enhancement, ultimately increasing

the light absorption of the active layer and improving the photovoltaic performance of the solar cell.

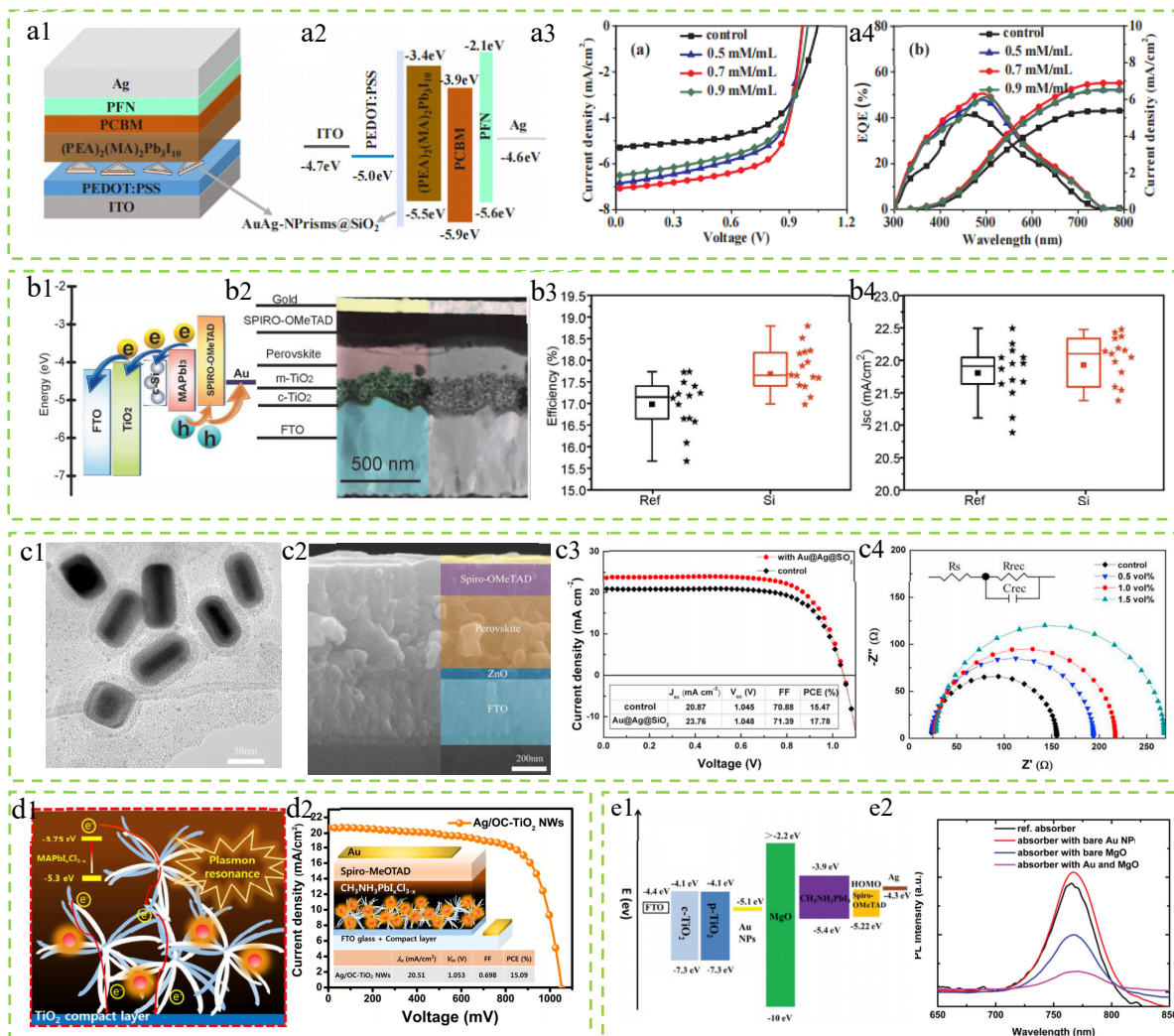


**Figure 8.** Summary of research for PSCs incorporating novel plasmonic nanomaterials. (a1–a4) AuAgNPrisms@SiO<sub>2</sub>: Reproduced with permission from Ref. [135]. Copyright 2019, Elsevier. (b1–b4) Si nanoparticles: Reproduced with permission from Ref. [136]. Copyright 2018, Wiley. (c1–c4) Au@Ag@SiO<sub>2</sub> core-shell nanocuboids: Reproduced with permission from Ref. [137]. Copyright 2019, Elsevier. (d1,d2) SiO<sub>2</sub>@Ag@OC-TiO<sub>2</sub> nanowires: Reproduced with permission from Ref. [138]. Copyright 2016, the Royal Society of Chemistry. (e1,e2) Au nanoparticles and MgO: Reproduced with permission from Ref. [139]. Copyright 2017, the Royal Society of Chemistry.

Au@Ag@SiO<sub>2</sub> core-shell nanocuboids (Au@Ag@SiO<sub>2</sub> NCs). Deng et al. successfully embedded Au@Ag@SiO<sub>2</sub> core-shell nanoparticles into the perovskite film of planar hetero-junction PSCs, which significantly increased the J<sub>SC</sub> [137]. The J<sub>SC</sub> of the original device is 20.87 mA/cm<sup>2</sup>, while the J<sub>SC</sub> with the addition of the Au@Ag@SiO<sub>2</sub> NC device increased to 23.76 mA/cm<sup>2</sup>, an increase of 13.85%. This is because the addition of nanoparticles enhances the induced light absorption and charge carrier separation capabilities, improving the performance of the device. Figure 8(c1,c2) show the TEM image of Au@Ag@SiO<sub>2</sub> NCs and SEM images of the cross-section of PSCs, with the size of the nanoparticles being 50 nm. Figure 8(c3) shows the J-V curves of the reference device and the device with added Au@Ag@SiO<sub>2</sub> NCs. It can be seen that the addition of nanocuboids effectively improved the performance of the photovoltaic device, with the best-performing device having J<sub>SC</sub> of 23.76 mA/cm<sup>2</sup>, V<sub>OC</sub> of 1.048 V, FF of 71.39%, and PCE of 17.78%. Figure 8(c4) presents

the Nyquist plots and simplified equivalent circuits of devices with different additional Au@Ag@SiO<sub>2</sub> nanoparticle content. The results show that the addition of nanoparticles reduces the carrier recombination rate and promotes charge separation and carrier transport, leading to an increase in  $V_{OC}$ .

SiO<sub>2</sub>@Ag@OC-TiO<sub>2</sub> nanowires (SiO<sub>2</sub>@Ag@OC-TiO<sub>2</sub> NWs). Yu et al. synthesized Ag@OC-TiO<sub>2</sub>NWs (SiO<sub>2</sub>@Ag@OC-TiO<sub>2</sub> NWs) composite material encapsulated with Si and incorporated it into the ETL of PSCs [138]. As shown in Figure 8(d1), the figure illustrates the electron transfer path in the PSCs with Ag@OC-TiO<sub>2</sub>NWs incorporated, as well as the plasmonic effect of Ag NPs decorated on OC-TiO<sub>2</sub>NWs. The LSPR and induced exciton dissociation mechanisms exhibited by Ag nanoparticles can significantly enhance the PCE of PSCs. Figure 8(d2) shows the optimal  $J-V$  curve of the PSCs after the incorporation of SiO<sub>2</sub>@Ag@OC-TiO<sub>2</sub>NWs, with the inset providing a schematic illustration of the structure of PSCs containing SiO<sub>2</sub>@Ag@OC-TiO<sub>2</sub>NWs. Due to the large pore structure in the OC-TiO<sub>2</sub>NWs, the permeability of the perovskite solution is enhanced, minimizing harmful voids in the ETL, which in turn achieves a higher  $V_{OC}$  and FF. Simultaneously, the plasma effect significantly enhances light absorption capabilities, and the increase in recombination resistance synergistically promotes the enhancement of current density. Ultimately, our research reveals that the PSCs based on the synergistic scaffold structure composed of Ag nanoparticles and OC-TiO<sub>2</sub>NWs exhibit exceptionally superior performance, achieving a PCE of up to 15.09%, marking a remarkable 24% enhancement compared to PSCs based on a scaffold layer of pure TiO<sub>2</sub> nanoparticles. Furthermore, the average PCE of these PSCs with the synergistic scaffold structure also reaches 12.17%, demonstrating good stability and consistency.

Au nanoparticles and MgO. Zhang et al. successfully fabricated solar cells by incorporating Au nanoparticles into mesoporous TiO<sub>2</sub> films and depositing a MgO passivation layer on the Au NP-modified mesoporous titanium substrate through a wet spinning process and the thermal decomposition of magnesium salt [139]. This approach aimed to enhance the performance of solar cells by improving interfacial properties and light absorption efficiency. The PSCs prepared by combining Au nanoparticles with MgO exhibit outstanding performance, with a PCE of up to 16.1%, a  $V_{OC}$  of up to 1.09 V, and a  $J_{SC}$  reaching 21.76 mA/cm<sup>2</sup>. Figure 8(e1) depicts the energy diagram of the materials in the PSCs containing Au nanoparticles and MgO. Figure 8(e2) shows the PL spectrum of the perovskite absorber layer with p-TiO<sub>2</sub> or MgO coating. It can be clearly seen from the data in the figure that the PL quenching degree of perovskite samples with magnesium salt as MgO coating is significantly enhanced. This phenomenon confirms that the electron extraction efficiency of perovskite modified by MgO on the TiO<sub>2</sub> layer is significantly higher than that of the original TiO<sub>2</sub>. Furthermore, when perovskite samples are simultaneously modified by Au nanoparticles and MgO, their PL peak intensity is reduced to the lowest, showing the most intense PL quenching effect. This indicates that the charge transfer process is significantly accelerated, effectively improving the electron extraction efficiency, reducing charge accumulation, and thus helping to increase the  $J_{SC}$  and overall photovoltaic performance of the device. Compared with devices based on pure TiO<sub>2</sub>, the PCE of the device has significantly increased by 34.2%. This enhancement may be closely related to the effective photon management generated by Au nanoparticles and MgO layers. This mechanism helps to reduce the photon and energy losses of charge carriers during the generation process, thereby enhancing the high charge transfer capability of PSCs and reducing charge recombination losses. In addition, by combining the use of Au NPs and insulating MgO layers in the passivation layer, the stability of PSC devices under ultraviolet light irradiation is significantly improved.

As shown in Table 2, a summary of the application of some plasma structures other than precious metals such as Au and Ag in PSCs is presented. This includes common metal Al, semiconductor material Si, and metal alloy nanomaterials Au-Ag and Cu-Ag, as well as some newly synthesized novel plasma structures such as AgOx@Ag nanoparticles, Au@PAT nanoparticles, etc.

**Table 2.** Summary of photovoltaic parameters for PSCs incorporating other plasmonic materials. (The numbers in parentheses indicate the reference device performance.)

| Materials                                     | Size              | Position of NPs                                  | $J_{SC}$<br>(mA/cm <sup>2</sup> ) | $V_{OC}$ (V) | FF (%)        | $\Delta FF$ (%) | PCE (%)       | $\Delta PCE$ (%) | Refs  |
|---|-------------------|--|-----------------------------------|--------------|---------------|-----------------|---------------|------------------|-------|
| Al NPs  | 20–70 nm          | Between ETL (PCBM) and electrode                 | 18.15 (16.71)                     | 0.97 (0.96)  | 67.40 (65.10) | 3.53            | 11.74 (10.54) | 11.39            | [126] |
| Au@Ag nanocuboids                             | 15 nm             | ETL(m-TiO <sub>2</sub> )                         | 23.60 (20.68)                     | 1.04 (1.00)  | 74.60 (73.00) | 2.19            | 18.31 (15.16) | 20.78            | [132] |
| Au-Ag alloy popcorns                          | 150 ± 50 nm       | ETL(m-TiO <sub>2</sub> )                         | 16.46 (15.51)                     | 0.95 (0.92)  | 66.00 (63.00) | 4.76            | 10.30 (8.90)  | 15.73            | [133] |
| AuAg@AuAg core-shell alloy nanocrystals       | 46 nm             | HTL (PEDOT: PSS)                                 | 21.89 (20.42)                     | 1.02 (0.95)  | 77.20 (71.60) | 7.82            | 16.76 (13.14) | 27.55            | [134] |
| AuAgNPrisms@SiO <sub>2</sub>                  | ~40 nm            | Between perovskite and HTL                       | 7.08 (5.33)                       | 0.97 (1.05)  | 67.00 (62.00) | 8.06            | 4.60 (3.43)   | 34.11            | [135] |
| Si NPs  | 140 nm            | Between perovskite and ETL                       | 22.40 (22.00)                     | 1.06 (1.05)  | 78.90 (77.00) | 2.47            | 18.80 (17.70) | 6.21             | [136] |
| Au@Ag@SiO <sub>2</sub> core-shell nanocuboids | 50 nm             | Perovskite                                       | 23.76 (20.87)                     | 1.05 (1.05)  | 71.39 (70.88) | 0.72            | 17.78 (15.47) | 14.93            | [137] |
| SiO <sub>2</sub> @Ag@OC-TiO <sub>2</sub> NW   | 400 nm            | ETL(TiO <sub>2</sub> )                           | 20.51 (19.36)                     | 1.05 (1.00)  | 69.80 (64.50) | 8.22            | 15.09 (12.54) | 20.33            | [138] |
| Au nanoparticles and MgO                      | 40 nm<br>(400 nm) | Between perovskite and ETL                       | 21.76 (19.49)                     | 1.09 (0.94)  | 68.00 (66.00) | 3.03            | 16.10 (12.00) | 34.17            | [139] |
| Au-Ag nanoalloy                               | 40 nm             | ETL(TiO <sub>2</sub> )                           | 21.75 (20.38)                     | 1.02 (1.03)  | 65.70 (63.90) | 2.82            | 14.42 (13.05) | 10.50            | [140] |
| Cu-Ag alloy NPs                               | 200 nm            | Between perovskite and electrode                 | 22.96 (—)                         | 1.12 (—)     | 73.20 (—)     | —               | 18.89 (13.68) | 38.08            | [141] |
| AgOx@Ag NPs                                   | 40 nm             | ETL(m-TiO <sub>2</sub> )                         | 23.35 (21.86)                     | 1.12 (1.09)  | 77.75 (75.00) | 3.67            | 20.33 (17.87) | 13.77            | [142] |
| Au@PAT NPs                                    | 22 nm             | MAPBI <sub>3</sub>                               | 21.71 (21.20)                     | 1.15 (1.12)  | 82.17 (78.00) | 5.35            | 20.52 (18.59) | 10.38            | [143] |
| Au/Ag NSs                                     | ~60 nm            | ETL(m-TiO <sub>2</sub> )                         | —                                 | —            | —             | —               | 4.90 (3.90)   | 25.64            | [144] |
| Submicron s-TiO <sub>2</sub> NPs              | 160 nm            | ETL(m-TiO <sub>2</sub> )                         | 21.61 (20.28)                     | 1.05 (1.08)  | 68.00 (67.00) | 1.49            | 16.72 (16.31) | 2.51             | [145] |
| Au@TiO <sub>2</sub> nanofibers                | 60 nm             | ETL  | 21.63 (19.14)                     | 0.99 (0.84)  | 70.00 (58.00) | 20.69           | 14.92 (9.23)  | 61.65            | [146] |
| Au nanorods@MgO                               | 12 nm<br>(40 nm)  | ETL (c-TiO <sub>2</sub> )                        | 22.35 (20.10)                     | 1.04 (1.02)  | 75.00 (72.00) | 4.17            | 17.40 (14.70) | 18.37            | [147] |
| Ge NPs  | 100 nm            | ETL (m-TiO <sub>2</sub> )                        | 22.93 (21.10)                     | 1.06 (1.08)  | 75.91 (71.42) | 6.29            | 18.59 (16.24) | 14.47            | [148] |
| GNR@SiO <sub>2</sub>                          | 55 nm             | Perovskite                                       | 24.25 (24.16)                     | 1.08 (1.06)  | 81.41 (79.24) | 2.74            | 23.26 (20.29) | 14.64            | [149] |
| SiO <sub>2</sub> @Ag@Ag <sub>2</sub> S NPs    | 120 nm            | Perovskite                                       | 24.66 (22.17)                     | 1.06 (1.06)  | 76.00 (74.30) | 2.29            | 19.88 (17.49) | 13.66            | [150] |
| TiN NPs                                       | 20 nm             | Perovskite                                       | 26.45 (25.09)                     | 1.06 (1.05)  | 76.07 (72.70) | 4.64            | 21.37 (19.07) | 12.06            | [151] |
| Au@SiO <sub>2</sub> @Graphene NPs             | 17 nm             | CH <sub>3</sub> NH <sub>3</sub> PbI <sub>3</sub> | 28.17 (21.20)                     | 1.00 (0.98)  | 71.00 (68.00) | 4.41            | 20.05 (14.21) | 41.10            | [152] |
| rGO NPs                                       | —                 | ETL  | 22.51 (21.01)                     | 1.06 (1.05)  | 72.00 (72.00) | 0.00            | 17.08 (15.93) | 7.22             | [153] |

#### 4. Conclusions and Outlook

This review provides a comprehensive summary of recent advancements in the enhancement of PSCs through the incorporation of plasmonic nanostructures. Initially, the analysis delves into four prominent manifestations of LSPR employed in photovoltaic devices: far-field scattering, near-field enhancement, HET, and PRET. Subsequently, the applications of MNPs—comprising precious metals such as Au and Ag and common metals like Al and Cu, as well as various alloys—are systematically reviewed and analyzed based on their types and shapes. The results demonstrate that incorporating MNPs with different LSPR properties into PSCs can effectively improve the efficiency and overall performance of these cells. However, despite the significant advancements made thus far, several issues and challenges remain to be addressed for the widespread commercialization of plasmonic-enhanced PSCs:

- (1) The selection of plasmonic materials that are both cost-effective and compatible with perovskite chemistry is crucial. At present, the primary materials employed are noble metals such as Au and Ag, which are both expensive and limited in supply. Consequently, there emerges an urgent imperative to scout and cultivate alternative materials that not only promise cost savings but are also abundant in nature. Al and Cu, albeit harboring potential as promising plasmonic materials, have been relatively neglected in the realm of research and application. Apart from these materials, we can develop a range of alternative plasmonic materials, such as transition metal materials, oxide materials, semiconductor materials, metal alloy materials, composite materials, and so on, to facilitate the further advancement of research on plasmonic solar cells. Moreover, the fabrication of plasmonic nanostructures encounters formidable challenges, encapsulated in substantial equipment expenditures, intricate manufacturing processes, substantial energy depletion, and the elusive pursuit of uniformity and stability. Therefore, the development of large-area, uniform, and scalable nanostructuring methods is essential. Techniques such as roll-to-roll nanoimprinting, nanosphere lithography, and colloidal self-assembly can enable the fabrication of plasmonic structures over large areas with high precision. Furthermore, research on hybrid plasmonic–dielectric structures can offer a balance between cost and performance.
- (2) A major hurdle that hinders the large-scale deployment of PSCs is their limited stability. Plasmonic nanostructures, while effective in boosting optical absorption and electron extraction, can also introduce additional interfaces and materials that can compromise the device's longevity. The degradation of perovskite materials under illumination, humidity, and temperature fluctuations is further exacerbated by the presence of plasmonic particles. Developing encapsulation techniques that effectively isolate the plasmonic–perovskite interface from environmental stressors is crucial. Researchers can also explore the use of more stable plasmonic materials or hybrid nanostructures that combine the benefits of multiple materials. Additionally, optimizing the perovskite composition and interface engineering can further improve the stability of PSCs.
- (3) There are potentially detrimental aspects of plasmonic nanomaterials for the performance of solar cells. Although plasmonic materials have shown remarkable advantages in improving the performance of solar cells, they can also bring some harmful effects, including the introduction of more defects, an increase in recombination centers, the generation of hotspots, the induction of material degradation, and environmental pollution. To fully leverage their advantages while mitigating the harmful impacts, continuous technological research and innovation, as well as the optimization of production processes and environmental protection measures, are essential for achieving sustainable development. By optimizing the synthesis methods of nanomaterials, controlling plasma treatment parameters, and improving device structures, we can maximize the benefits of plasma nanomaterials while minimizing their adverse effects on solar cell performance.

- (4) Most research on plasmonic-enhanced PSCs has focused on laboratory-scale devices with small active areas. As the device size increases, challenges arise due to non-uniform distribution of light, plasmonic hotspots, and increased resistance losses, resulting in a significant drop in the overall efficiency. Future research should focus on integrating plasmonic-enhanced PSCs into larger photovoltaic systems, considering factors such as module design, interconnection strategies, and overall system optimization. This includes developing methods to mitigate efficiency losses in large-area devices and optimizing the integration of PSCs with other photovoltaic technologies, such as silicon-based cells, in tandem or multi-junction configurations.
- (5) We could consider integrating plasmonic technology with cutting-edge innovative technologies such as artificial intelligence (AI) and machine learning [154]. For instance, by leveraging big data analysis and machine learning algorithms, we can swiftly screen and predict potential novel materials in plasmonic technology [155]; with the assistance of AI's optimization algorithms, we can fine-tune the plasmonic process parameters to achieve customized material properties [156]; AI's formidable data processing capabilities enable it to explore material combinations and process conditions that are difficult to reach with traditional methods [157,158]. In this way, we can not only enhance material research and development efficiency, optimize material performance, and facilitate the discovery of new materials but also improve equipment performance, achieve intelligent control, and optimize process flows, thereby accelerating technological innovation, boosting industrial competitiveness, and promoting sustainable development.

In summary, the integration of plasmonic structures in PSCs represents a significant step forward in the pursuit of highly efficient and stable photovoltaic devices. With continued research and innovation, it is anticipated that plasmonics will play an increasingly important role in the transition towards sustainable and renewable energy sources, ultimately contributing to a greener and more sustainable future.

**Author Contributions:** C.W. collated documents and wrote the manuscript; X.W. and X.S. (Xiangqian Shen) collaborated with the selection, preparation, and revision of the manuscript; B.L. and X.S. (Xiaohao Shi) polished the language; X.S. (Xiangqian Shen) and C.W. collaborated in the revision of the manuscript. All authors have read and agreed to the published version of the manuscript.

**Funding:** This project was supported by the Natural Science Foundation of Xinjiang Uygur Autonomous Region of China (grant No. 2022D01C20), the Tianshan Innovation Team Program of Xinjiang Uygur Autonomous Region of China (grant No. 2023D14001), and the National Natural Science Foundation of China (grant No. 12164047).

**Institutional Review Board Statement:** Not applicable.

**Informed Consent Statement:** Not applicable.

**Data Availability Statement:** Data are contained within the article.

**Conflicts of Interest:** Author Xiaodan Wang was employed by the company Helmholtz-Zentrum Berlin für Materialien und Energie GmbH. The remaining authors declare that the research was conducted in the absence of any commercial or financial relationships that could be construed as a potential conflict of interest.

## References

1. Koroneos, C.; Spachos, T.; Moussiopoulos, N. Exergy analysis of renewable energy sources. *Renew. Energy* **2003**, *28*, 295–310. [[CrossRef](#)]
2. Panwar, N.L.; Kaushik, S.C.; Kothari, S. Role of renewable energy sources in environmental protection: A review. *Renew. Sustain. Energy Rev.* **2011**, *15*, 1513–1524. [[CrossRef](#)]
3. Yuan, S.-Y.; Zhao, H.; Wang, Y.-T.; Li, Z.-Z.; Wang, X.-D.; Cao, W.-P. Research status of all-inorganic perovskite solar cells: A review. *J. Solid State Chem.* **2023**, *328*, 124299. [[CrossRef](#)]
4. Barker, P.P.; Bing, J.M. Advances in solar photovoltaic technology: An applications perspective. In Proceedings of the IEEE Power Engineering Society General Meeting, San Francisco, CA, USA, 16 June 2005; pp. 1955–1960.

5. Hu, Y.; Schlipf, J.; Wussler, M.; Petrus, M.L.; Jaegermann, W.; Bein, T.; Müller-Buschbaum, P.; Docampo, P. Hybrid Perovskite/Perovskite Heterojunction Solar Cells. *ACS Nano* **2016**, *10*, 5999–6007. [[CrossRef](#)] [[PubMed](#)]
6. Liu, T.; Chen, K.; Hu, Q.; Zhu, R.; Gong, Q. Inverted Perovskite Solar Cells: Progresses and Perspectives. *Adv. Energy Mater.* **2016**, *6*, 1600457. [[CrossRef](#)]
7. Lal, N.N.; Dkhissi, Y.; Li, W.; Hou, Q.; Cheng, Y.B.; Bach, U. Perovskite Tandem Solar Cells. *Adv. Energy Mater.* **2017**, *7*, 1602761. [[CrossRef](#)]
8. Wang, R.; Mujahid, M.; Duan, Y.; Wang, Z.K.; Xue, J.; Yang, Y. A Review of Perovskites Solar Cell Stability. *Adv. Funct. Mater.* **2019**, *29*, 1808843. [[CrossRef](#)]
9. Jiang, Z.; Wang, B.; Zhang, W.; Yang, Z.; Li, M.; Ren, F.; Imran, T.; Sun, Z.; Zhang, S.; Zhang, Y.; et al. Solvent engineering towards scalable fabrication of high-quality perovskite films for efficient solar modules. *J. Energy Chem.* **2023**, *80*, 689–710. [[CrossRef](#)]
10. Raza, H.; Imran, T.; Gao, Y.; Azeem, M.; Younis, M.; Wang, J.; Liu, S.; Yang, Z.; Liu, Z.; Chen, W. Potential-induced degradation: A challenge in the commercialization of perovskite solar cells. *Energy Environ. Sci.* **2024**, *17*, 1819–1853. [[CrossRef](#)]
11. Jiang, Z.-Y.; Pan, M.; Ren, F.-M.; Chen, R.; Sun, Z.-X.; Yang, Z.-C.; Liu, Z.-H.; Chen, W. Boosting stability of inverted perovskite solar cells with magnetron-sputtered molybdenum rear electrodes. *Rare Met.* **2023**, *42*, 3741–3754. [[CrossRef](#)]
12. Kaltenbrunner, M.; White, M.S.; Glowacki, E.D.; Sekitani, T.; Someya, T.; Sariciftci, N.S.; Bauer, S. Ultrathin and lightweight organic solar cells with high flexibility. *Nat. Commun.* **2012**, *3*, 770. [[CrossRef](#)] [[PubMed](#)]
13. Min, H.; Kim, M.; Lee, S.-U.; Kim, H.; Kim, G.; Choi, K.; Lee, J.H.; Seok, S.I. Efficient, stable solar cells by using inherent bandgap of  $\alpha$ -phase formamidinium lead iodide. *Science* **2019**, *366*, 749–753. [[CrossRef](#)] [[PubMed](#)]
14. Ou, X.-L.; Xu, M.; Feng, J.; Sun, H.-B. Flexible and efficient ITO-free semitransparent perovskite solar cells. *Sol. Energy Mater. Sol. Cells* **2016**, *157*, 660–665. [[CrossRef](#)]
15. Liu, M.; Johnston, M.B.; Snaith, H.J. Efficient planar heterojunction perovskite solar cells by vapour deposition. *Nature* **2013**, *501*, 395–398. [[CrossRef](#)] [[PubMed](#)]
16. Nakazaki, J.; Segawa, H. Evolution of organometal halide solar cells. *J. Photochem. Photobiol. C Photochem. Rev.* **2018**, *35*, 74–107. [[CrossRef](#)]
17. Pérez-del-Rey, D.; Forgács, D.; Hutter, E.M.; Savenije, T.J.; Nordlund, D.; Schulz, P.; Berry, J.J.; Sessolo, M.; Bolink, H.J. Strontium Insertion in Methylammonium Lead Iodide: Long Charge Carrier Lifetime and High Fill-Factor Solar Cells. *Adv. Mater.* **2016**, *28*, 9839–9845. [[CrossRef](#)]
18. Yang, W.S.; Park, B.-W.; Jung, E.H.; Jeon, N.J.; Kim, Y.C.; Lee, D.U.; Shin, S.S.; Seo, J.; Kim, E.K.; Noh, J.H.; et al. Iodide management in formamidinium-lead-halide-based perovskite layers for efficient solar cells. *Science* **2017**, *356*, 1376–1379. [[CrossRef](#)]
19. Shi, S.; Li, Y.; Li, X.; Wang, H. Advancements in all-solid-state hybrid solar cells based on organometal halide perovskites. *Mater. Horiz.* **2015**, *2*, 378–405. [[CrossRef](#)]
20. Chen, J.; Park, N.G. Causes and Solutions of Recombination in Perovskite Solar Cells. *Adv. Mater.* **2018**, *31*, 1803019. [[CrossRef](#)]
21. Zhou, H.; Chen, Q.; Li, G.; Luo, S.; Song, T.-b.; Duan, H.-S.; Hong, Z.; You, J.; Liu, Y.; Yang, Y. Interface engineering of highly efficient perovskite solar cells. *Science* **2014**, *345*, 542–546. [[CrossRef](#)]
22. Jeon, N.J.; Noh, J.H.; Yang, W.S.; Kim, Y.C.; Ryu, S.; Seo, J.; Seok, S.I. Compositional engineering of perovskite materials for high-performance solar cells. *Nature* **2015**, *517*, 476–480. [[CrossRef](#)] [[PubMed](#)]
23. Kim, J.Y.; Lee, J.-W.; Jung, H.S.; Shin, H.; Park, N.-G. High-Efficiency Perovskite Solar Cells. *Chem. Rev.* **2020**, *120*, 7867–7918. [[CrossRef](#)]
24. Hodes, G.; Cahen, D. Perovskite cells roll forward. *Nat. Photonics* **2014**, *8*, 87–88. [[CrossRef](#)]
25. Kim, H.-S.; Im, S.H.; Park, N.-G. Organolead Halide Perovskite: New Horizons in Solar Cell Research. *J. Phys. Chem. C* **2014**, *118*, 5615–5625. [[CrossRef](#)]
26. Roy, P.; Kumar Sinha, N.; Tiwari, S.; Khare, A. A review on perovskite solar cells: Evolution of architecture, fabrication techniques, commercialization issues and status. *Sol. Energy* **2020**, *198*, 665–688. [[CrossRef](#)]
27. Liu, K.; Rafique, S.; Musolino, S.F.; Cai, Z.; Liu, F.; Li, X.; Yuan, Y.; Bao, Q.; Yang, Y.; Chu, J.; et al. Covalent bonding strategy to enable non-volatile organic cation perovskite for highly stable and efficient solar cells. *Joule* **2023**, *7*, 1033–1050. [[CrossRef](#)]
28. Zhao, Y.; Ma, F.; Qu, Z.; Yu, S.; Shen, T.; Deng, H.-X.; Chu, X.; Peng, X.; Yuan, Y.; Zhang, X.; et al. Inactive (PbI<sub>2</sub>)<sub>2</sub>RbCl stabilizes perovskite films for efficient solar cells. *Science* **2022**, *377*, 531–534. [[CrossRef](#)] [[PubMed](#)]
29. Guo, P.; Dong, J.; Xu, C.; Yao, Y.; You, J.; Bian, H.; Zeng, W.; Zhou, G.; He, X.; Wang, M.; et al. Fabrication of an ultrathin PEG-modified PEDOT:PSS HTL for high-efficiency Sn–Pb perovskite solar cells by an eco-friendly solvent etching technique. *J. Mater. Chem. A* **2023**, *11*, 7246–7255. [[CrossRef](#)]
30. You, J.; Bian, H.; Wang, M.; Cai, X.; Li, C.; Zhou, G.; Lu, H.; Fang, C.; Huang, J.; Yao, Y.; et al. Eco-friendly glucose assisted structurally simplified high-efficiency tin-lead mixed perovskite solar cells. *J. Energy Chem.* **2023**, *85*, 83–90. [[CrossRef](#)]
31. Shen, X.; Lin, X.; Peng, Y.; Zhang, Y.; Long, F.; Han, Q.; Wang, Y.; Han, L. Two-Dimensional Materials for Highly Efficient and Stable Perovskite Solar Cells. *Nano-Micro Lett.* **2024**, *16*, 201. [[CrossRef](#)]
32. Xing, J.; Sun, Y.; He, S.; Huang, X.; Li, Y.; Huang, Z.; Wang, B.; Zhou, R.; Li, Y.; Zhang, J.; et al. Triple-Cation Mixed-Halide Perovskite Single-Crystal Thin-Film for High-Performance Photodetector via Adjusting Lattice Strain and Mitigating Surface Defects. *Adv. Funct. Mater.* **2024**, 2411619. [[CrossRef](#)]

33. Stranks, S.D.; Eperon, G.E.; Grancini, G.; Menelaou, C.; Alcocer, M.J.P.; Leijtens, T.; Herz, L.M.; Petrozza, A.; Snaith, H.J. Electron-Hole Diffusion Lengths Exceeding 1 Micrometer in an Organometal Trihalide Perovskite Absorber. *Science* **2013**, *342*, 341–344. [[CrossRef](#)]
34. Wehrenfennig, C.; Eperon, G.E.; Johnston, M.B.; Snaith, H.J.; Herz, L.M. High Charge Carrier Mobilities and Lifetimes in Organolead Trihalide Perovskites. *Adv. Mater.* **2013**, *26*, 1584–1589. [[CrossRef](#)] [[PubMed](#)]
35. Kojima, A.; Teshima, K.; Shirai, Y.; Miyasaka, T. Organometal Halide Perovskites as Visible-Light Sensitizers for Photovoltaic Cells. *J. Am. Chem. Soc.* **2009**, *131*, 6050–6051. [[CrossRef](#)] [[PubMed](#)]
36. Mei, A.; Li, X.; Liu, L.; Ku, Z.; Liu, T.; Rong, Y.; Xu, M.; Hu, M.; Chen, J.; Yang, Y.; et al. A hole-conductor-free, fully printable mesoscopic perovskite solar cell with high stability. *Science* **2014**, *345*, 295–298. [[CrossRef](#)]
37. Berhe, T.A.; Su, W.-N.; Chen, C.-H.; Pan, C.-J.; Cheng, J.-H.; Chen, H.-M.; Tsai, M.-C.; Chen, L.-Y.; Dubale, A.A.; Hwang, B.-J. Organometal halide perovskite solar cells: Degradation and stability. *Energy Environ. Sci.* **2016**, *9*, 323–356. [[CrossRef](#)]
38. Leijtens, T.; Eperon, G.E.; Noel, N.K.; Habisreutinger, S.N.; Petrozza, A.; Snaith, H.J. Stability of Metal Halide Perovskite Solar Cells. *Adv. Energy Mater.* **2015**, *5*, 1500963. [[CrossRef](#)]
39. Wang, Q.; Phung, N.; Di Girolamo, D.; Vivo, P.; Abate, A. Enhancement in lifespan of halide perovskite solar cells. *Energy Environ. Sci.* **2019**, *12*, 865–886. [[CrossRef](#)]
40. Niu, G.; Guo, X.; Wang, L. Review of recent progress in chemical stability of perovskite solar cells. *J. Mater. Chem. A* **2015**, *3*, 8970–8980. [[CrossRef](#)]
41. Christians, J.A.; Schulz, P.; Tinkham, J.S.; Schloemer, T.H.; Harvey, S.P.; Tremolet de Villers, B.J.; Sellinger, A.; Berry, J.J.; Luther, J.M. Tailored interfaces of unencapsulated perovskite solar cells for >1000 hour operational stability. *Nat. Energy* **2018**, *3*, 68–74. [[CrossRef](#)]
42. Chan, K.; Wright, M.; Elumalai, N.; Uddin, A.; Pillai, S. Plasmonics in Organic and Perovskite Solar Cells: Optical and Electrical Effects. *Adv. Opt. Mater.* **2016**, *5*, 1600698. [[CrossRef](#)]
43. Siavash Moakhar, R.; Gholipour, S.; Masudy-Panah, S.; Seza, A.; Mehdikhani, A.; Riahi-Noori, N.; Tafazoli, S.; Timasi, N.; Lim, Y.F.; Saliba, M. Recent Advances in Plasmonic Perovskite Solar Cells. *Adv. Sci.* **2020**, *7*, 1902448. [[CrossRef](#)] [[PubMed](#)]
44. Li, Y.-F.; Kou, Z.-L.; Feng, J.; Sun, H.-B. Plasmon-enhanced organic and perovskite solar cells with metal nanoparticles. *Nanophotonics* **2020**, *9*, 3111–3133. [[CrossRef](#)]
45. Atwater, H.A. The promise of plasmonics. *Sci. Am.* **2007**, *296*, 56–63. [[CrossRef](#)] [[PubMed](#)]
46. Kasani, S.; Curtin, K.; Wu, N. A review of 2D and 3D plasmonic nanostructure array patterns: Fabrication, light management and sensing applications. *Nanophotonics* **2019**, *8*, 2065–2089. [[CrossRef](#)]
47. Ai, B.; Fan, Z.; Wong, Z.J. Plasmonic-perovskite solar cells, light emitters, and sensors. *Microsyst. Nanoeng.* **2022**, *8*, 5. [[CrossRef](#)]
48. Guo, Y.; He, X.; Liu, X.; Li, X.; Kang, L. One-step implementation of plasmon enhancement and solvent annealing effects for air-processed high-efficiency perovskite solar cells. *J. Mater. Chem. A* **2018**, *6*, 24036–24044. [[CrossRef](#)]
49. Higgins, M.; Ely, F.; Nome, R.C.; Nome, R.A.; dos Santos, D.P.; Choi, H.; Nam, S.; Quevedo-Lopez, M. Enhanced reproducibility of planar perovskite solar cells by fullerene doping with silver nanoparticles. *J. Appl. Phys.* **2018**, *124*, 065306. [[CrossRef](#)]
50. Kakavelakis, G.; Alexaki, K.; Stratakis, E.; Kymakis, E. Efficiency and stability enhancement of inverted perovskite solar cells via the addition of metal nanoparticles in the hole transport layer. *RSC Adv.* **2017**, *7*, 12998–13002. [[CrossRef](#)]
51. Hopper, E.R.; Boukouvala, C.; Asselin, J.; Biggins, J.S.; Ringe, E. Opportunities and Challenges for Alternative Nanoplasmonic Metals: Magnesium and Beyond. *J. Phys. Chem. C* **2022**, *126*, 10630–10643. [[CrossRef](#)]
52. Gutiérrez, Y.; Alcaraz de la Osa, R.; Ortiz, D.; Saiz, J.; González, F.; Moreno, F. Plasmonics in the Ultraviolet with Aluminum, Gallium, Magnesium and Rhodium. *Appl. Sci.* **2018**, *8*, 64. [[CrossRef](#)]
53. Yu, H.; Zhang, P.; Lu, S.; Yang, S.; Peng, F.; Chang, W.-S.; Liu, K. Synthesis and Multipole Plasmon Resonances of Spherical Aluminum Nanoparticles. *J. Phys. Chem. Lett.* **2020**, *11*, 5836–5843. [[CrossRef](#)]
54. Jacobson, C.R.; Solti, D.; Renard, D.; Yuan, L.; Lou, M.; Halas, N.J. Shining Light on Aluminum Nanoparticle Synthesis. *Acc. Chem. Res.* **2020**, *53*, 2020–2030. [[CrossRef](#)]
55. Ringe, E. Shapes, Plasmonic Properties, and Reactivity of Magnesium Nanoparticles. *J. Phys. Chem. C* **2020**, *124*, 15665–15679. [[CrossRef](#)] [[PubMed](#)]
56. Li, Z.; Kuroski, D. Plasmon-Driven Chemistry on Mono- and Bimetallic Nanostructures. *Acc. Chem. Res.* **2021**, *54*, 2477–2487. [[CrossRef](#)] [[PubMed](#)]
57. Lomonosov, V.; Yang, J.; Fan, Y.; Hofmann, S.; Ringe, E. Stability of Plasmonic Mg-MgO Core-Shell Nanoparticles in Gas-Phase Oxidative Environments. *Nano Lett.* **2024**, *24*, 7084–7090. [[CrossRef](#)]
58. Kakavelakis, G.; Petridis, K.; Kymakis, E. Recent advances in plasmonic metal and rare-earth-element upconversion nanoparticle doped perovskite solar cells. *J. Mater. Chem. A* **2017**, *5*, 21604–21624. [[CrossRef](#)]
59. Ijaz, M.; Shoukat, A.; Ayub, A.; Tabassum, H.; Naseer, H.; Tanveer, R.; Islam, A.; Iqbal, T. Perovskite solar cells: Importance, challenges, and plasmonic enhancement. *Int. J. Green Energy* **2020**, *17*, 1022–1035. [[CrossRef](#)]
60. Wang, H.; Brandl, D.W.; Nordlander, P.; Halas, N.J. Plasmonic Nanostructures: Artificial Molecules. *Acc. Chem. Res.* **2007**, *40*, 53–62. [[CrossRef](#)]
61. West, P.R.; Ishii, S.; Naik, G.V.; Emani, N.K.; Shalae, V.M.; Boltasseva, A. Searching for better plasmonic materials. *Laser Photonics Rev.* **2010**, *4*, 795–808. [[CrossRef](#)]

62. Sun, L.; Zhang, R.; Du, C.; Rong, W.; Li, X.; Shi, D. Enhanced photocurrent of perovskite solar cells by a layer of randomly-distributed-Ag-nanospheres. *Phys. Lett. A* **2021**, *414*, 127620. [[CrossRef](#)]
63. Tang, M.; Zhou, L.; Gu, S.; Zhu, W.; Wang, Y.; Xu, J.; Deng, Z.; Yu, T.; Lu, Z.; Zhu, J. Fine-tuning the metallic core-shell nanostructures for plasmonic perovskite solar cells. *Appl. Phys. Lett.* **2016**, *109*, 183901. [[CrossRef](#)]
64. Hui, Y.; You, E.-M.; Luo, Q.-P.; Wang, T.; Nan, Z.-A.; Gu, Y.; Zhang, W.-H.; Cai, Z.-Y.; Chen, L.; Zhou, J.-Z.; et al. Efficient plasmon-enhanced perovskite solar cells by molecularly isolated gold nanorods. *J. Energy Chem.* **2022**, *73*, 60–67. [[CrossRef](#)]
65. Batmunkh, M.; Macdonald, T.J.; Peveler, W.J.; Bati, A.S.R.; Carmalt, C.J.; Parkin, I.P.; Shapter, J.G. Plasmonic Gold Nanostars Incorporated into High-Efficiency Perovskite Solar Cells. *ChemSusChem* **2017**, *10*, 3750–3753. [[CrossRef](#)]
66. Li, S.; Zhu, X.; Wang, B.; Qiao, Y.; Liu, W.; Yang, H.; Liu, N.; Chen, M.; Lu, H.; Yang, Y. Influence of Ag Nanoparticles with Different Sizes and Concentrations Embedded in a TiO<sub>2</sub> Compact Layer on the Conversion Efficiency of Perovskite Solar Cells. *Nanoscale Res. Lett.* **2018**, *13*, 183901. [[CrossRef](#)]
67. Wang, D.; Chan, K.H.; Elumalai, N.K.; Mahmud, M.A.; Upama, M.B.; Uddin, A.; Pillai, S. Interfacial engineering of hole transport layers with metal and dielectric nanoparticles for efficient perovskite solar cells. *Phys. Chem. Chem. Phys.* **2017**, *19*, 25016–25024. [[CrossRef](#)]
68. Cui, J.; Chen, C.; Han, J.; Cao, K.; Zhang, W.; Shen, Y.; Wang, M. Surface Plasmon Resonance Effect in Inverted Perovskite Solar Cells. *Adv. Sci.* **2016**, *3*, 1500312. [[CrossRef](#)]
69. Kelly, K.L.; Coronado, E.; Zhao, L.L.; Schatz, G.C. The Optical Properties of Metal Nanoparticles: The Influence of Size, Shape, and Dielectric Environment. *J. Phys. Chem. B* **2003**, *107*, 668–677. [[CrossRef](#)]
70. Atwater, H.A.; Polman, A. Plasmonics for improved photovoltaic devices. *Nat. Mater.* **2010**, *9*, 205–213. [[CrossRef](#)]
71. Jang, Y.H.; Jang, Y.J.; Kim, S.; Quan, L.N.; Chung, K.; Kim, D.H. Plasmonic Solar Cells: From Rational Design to Mechanism Overview. *Chem. Rev.* **2016**, *116*, 14982–15034. [[CrossRef](#)]
72. Erwin, W.R.; Zarick, H.F.; Talbert, E.M.; Bardhan, R. Light trapping in mesoporous solar cells with plasmonic nanostructures. *Energy Environ. Sci.* **2016**, *9*, 1577–1601. [[CrossRef](#)]
73. Akimov, Y.A.; Koh, W.S.; Sian, S.Y.; Ren, S. Nanoparticle-enhanced thin film solar cells: Metallic or dielectric nanoparticles? *Appl. Phys. Lett.* **2010**, *96*, 073111. [[CrossRef](#)]
74. Thrithamarassery Gangadharan, D.; Xu, Z.; Liu, Y.; Izquierdo, R.; Ma, D. Recent advancements in plasmon-enhanced promising third-generation solar cells. *Nanophotonics* **2017**, *6*, 153–175. [[CrossRef](#)]
75. Zayats, A.V.; Smolyaninov, I.I.; Maradudin, A.A. Nano-optics of surface plasmon polaritons. *Phys. Rep.* **2005**, *408*, 131–314. [[CrossRef](#)]
76. Schuller, J.A.; Barnard, E.S.; Cai, W.; Jun, Y.C.; White, J.S.; Brongersma, M.L. Plasmonics for extreme light concentration and manipulation. *Nat. Mater.* **2010**, *9*, 193–204. [[CrossRef](#)]
77. Chen, C.; Zheng, S.; Song, H. Photon management to reduce energy loss in perovskite solar cells. *Chem. Soc. Rev.* **2021**, *50*, 7250–7329. [[CrossRef](#)] [[PubMed](#)]
78. Green, M.A.; Pillai, S. Harnessing plasmonics for solar cells. *Nat. Photonics* **2012**, *6*, 130–132. [[CrossRef](#)]
79. Spurio, E.; Pelli Cresi, J.S.; Ammirati, G.; Pelatti, S.; Paladini, A.; D’Addato, S.; Turchini, S.; O’Keeffe, P.; Catone, D.; Luches, P. Injecting Electrons into CeO<sub>2</sub> via Photoexcitation of Embedded Au Nanoparticles. *ACS Photonics* **2023**, *10*, 1566–1574. [[CrossRef](#)] [[PubMed](#)]
80. Wu, N. Plasmonic metal–semiconductor photocatalysts and photoelectrochemical cells: A review. *Nanoscale* **2018**, *10*, 2679–2696. [[CrossRef](#)]
81. Zhang, Y.; He, S.; Guo, W.; Hu, Y.; Huang, J.; Mulcahy, J.R.; Wei, W.D. Surface-Plasmon-Driven Hot Electron Photochemistry. *Chem. Rev.* **2017**, *118*, 2927–2954. [[CrossRef](#)]
82. Ferry, V.E.; Sweatlock, L.A.; Pacifici, D.; Atwater, H.A. Plasmonic Nanostructure Design for Efficient Light Coupling into Solar Cells. *Nano Lett.* **2008**, *8*, 4391–4397. [[CrossRef](#)] [[PubMed](#)]
83. Ferry, V.E.; Verschuuren, M.A.; Li, H.B.T.; Schropp, R.E.I.; Atwater, H.A.; Polman, A. Improved red-response in thin film a-Si:H solar cells with soft-imprinted plasmonic back reflectors. *Appl. Phys. Lett.* **2009**, *95*, 183503. [[CrossRef](#)]
84. Tan, S.; Argondizzo, A.; Ren, J.; Liu, L.; Zhao, J.; Petek, H. Plasmonic coupling at a metal/semiconductor interface. *Nat. Photonics* **2017**, *11*, 806–812. [[CrossRef](#)]
85. Wu, K.; Chen, J.; McBride, J.R.; Lian, T. Efficient hot-electron transfer by a plasmon-induced interfacial charge-transfer transition. *Science* **2015**, *349*, 632–635. [[CrossRef](#)] [[PubMed](#)]
86. Zhu, J.; Hsu, C.-M.; Yu, Z.; Fan, S.; Cui, Y. Nanodome Solar Cells with Efficient Light Management and Self-Cleaning. *Nano Lett.* **2009**, *10*, 1979–1984. [[CrossRef](#)]
87. Munday, J.N.; Atwater, H.A. Large Integrated Absorption Enhancement in Plasmonic Solar Cells by Combining Metallic Gratings and Antireflection Coatings. *Nano Lett.* **2010**, *11*, 2195–2201. [[CrossRef](#)]
88. Naik, G.V.; Schroeder, J.L.; Ni, X.; Kildishev, A.V.; Sands, T.D.; Boltasseva, A. Titanium nitride as a plasmonic material for visible and near-infrared wavelengths. *Opt. Mater. Express* **2012**, *2*, 478–489. [[CrossRef](#)]
89. Naik, G.V.; Shalae, V.M.; Boltasseva, A. Alternative Plasmonic Materials: Beyond Gold and Silver. *Adv. Mater.* **2013**, *25*, 3264–3294. [[CrossRef](#)]
90. Wiley, B.; Sun, Y.; Mayers, B.; Xia, Y. Shape-Controlled Synthesis of Metal Nanostructures: The Case of Silver. *Chem.—A Eur. J.* **2004**, *11*, 454–463. [[CrossRef](#)]

91. Yun, J.; Hwang, S.H.; Jang, J. Fabrication of Au@Ag Core/Shell Nanoparticles Decorated TiO<sub>2</sub> Hollow Structure for Efficient Light-Harvesting in Dye-Sensitized Solar Cells. *ACS Appl. Mater. Interfaces* **2015**, *7*, 2055–2063. [[CrossRef](#)]
92. Lee, K.-S.; El-Sayed, M.A. Gold and Silver Nanoparticles in Sensing and Imaging: Sensitivity of Plasmon Response to Size, Shape, and Metal Composition. *J. Phys. Chem. B* **2006**, *110*, 19220–19225. [[CrossRef](#)] [[PubMed](#)]
93. Lee, K.-S.; El-Sayed, M.A. Dependence of the Enhanced Optical Scattering Efficiency Relative to That of Absorption for Gold Metal Nanorods on Aspect Ratio, Size, End-Cap Shape, and Medium Refractive Index. *J. Phys. Chem. B* **2005**, *109*, 20331–20338. [[CrossRef](#)] [[PubMed](#)]
94. Yang, D.; Jang, J.G.; Lim, J.; Lee, J.-K.; Kim, S.H.; Hong, J.-I. Correlations of Optical Absorption, Charge Trapping, and Surface Roughness of TiO<sub>2</sub> Photoanode Layer Loaded with Neat Ag-NPs for Efficient Perovskite Solar Cells. *ACS Appl. Mater. Interfaces* **2016**, *8*, 21522–21530. [[CrossRef](#)] [[PubMed](#)]
95. Hsu, H.-L.; Juang, T.-Y.; Chen, C.-P.; Hsieh, C.-M.; Yang, C.-C.; Huang, C.-L.; Jeng, R.-J. Enhanced efficiency of organic and perovskite photovoltaics from shape-dependent broadband plasmonic effects of silver nanoplates. *Sol. Energy Mater. Sol. Cells* **2015**, *140*, 224–231. [[CrossRef](#)]
96. Liu, S.; Liang, L.; Meng, L.; Tian, X.; Zhang, Z.; Yu, Y.; Lan, Z.; Wu, J.; Zhang, J.; Gao, P. Synergy of plasmonic silver nanorod and water for enhanced planar perovskite photovoltaic devices. *Sol. Rrl* **2019**, *4*, 1900231. [[CrossRef](#)]
97. Nourolahi, H.; Behjat, A.; Hosseini Zarch, S.M.M.; Bolorizadeh, M.A. Silver nanoparticle plasmonic effects on hole-transport material-free mesoporous heterojunction perovskite solar cells. *Sol. Energy* **2016**, *139*, 475–483. [[CrossRef](#)]
98. Kim, G.M.; Tatsuma, T. Photocurrent Enhancement of Perovskite Solar Cells at the Absorption Edge by Electrode-Coupled Plasmons of Silver Nanocubes. *J. Phys. Chem. C* **2017**, *121*, 11693–11699. [[CrossRef](#)]
99. Ali, A.; Kang, J.H.; Seo, J.H.; Walker, B. Effect of Plasmonic Ag Nanoparticles on the Performance of Inverted Perovskite Solar Cells. *Adv. Eng. Mater.* **2019**, *22*, 1900976. [[CrossRef](#)]
100. Yao, K.; Zhong, H.; Liu, Z.; Xiong, M.; Leng, S.; Zhang, J.; Xu, Y.-X.; Wang, W.; Zhou, L.; Huang, H.; et al. Plasmonic Metal Nanoparticles with Core–Bishell Structure for High-Performance Organic and Perovskite Solar Cells. *ACS Nano* **2019**, *13*, 5397–5409. [[CrossRef](#)]
101. Saliba, M.; Zhang, W.; Burlakov, V.M.; Stranks, S.D.; Sun, Y.; Ball, J.M.; Johnston, M.B.; Goriely, A.; Wiesner, U.; Snaith, H.J. Plasmonic-Induced Photon Recycling in Metal Halide Perovskite Solar Cells. *Adv. Funct. Mater.* **2015**, *25*, 5038–5046. [[CrossRef](#)]
102. Wang, B.; Zhu, X.; Li, S.; Chen, M.; Lu, H.; Yang, Y. Ag@SiO<sub>2</sub> Core-shell Nanoparticles Embedded in a TiO<sub>2</sub> Mesoporous Layer Substantially Improve the Performance of Perovskite Solar Cells. *Nanomaterials* **2018**, *8*, 701. [[CrossRef](#)] [[PubMed](#)]
103. Wu, Y.; Chen, C.; Wang, H.; Bi, W.; Song, Z.; Chen, X.; Jin, J.; Chen, X.; Xu, L.; Dai, Q.; et al. Toward ultra-thin and full functional perovskite solar cells by broadband light scattering management and efficient interfacial modification. *Sol. Energy Mater. Sol. Cells* **2020**, *206*, 110297. [[CrossRef](#)]
104. Gao, Y.; Zhang, J.; Zhang, Z.; Li, Z.; Xiong, Q.; Deng, L.; Zhou, Q.; Meng, L.; Du, Y.; Zuo, T.; et al. Plasmon-Enhanced Perovskite Solar Cells with Efficiency Beyond 21 %: The Asynchronous Synergistic Effect of Water and Gold Nanorods. *ChemPlusChem* **2021**, *86*, 291–297. [[CrossRef](#)]
105. Lee, D.S.; Kim, W.; Cha, B.G.; Kwon, J.; Kim, S.J.; Kim, M.; Kim, J.; Wang, D.H.; Park, J.H. Self-Position of Au NPs in Perovskite Solar Cells: Optical and Electrical Contribution. *ACS Appl. Mater. Interfaces* **2015**, *8*, 449–454. [[CrossRef](#)] [[PubMed](#)]
106. Ghahremanirad, E.; Olyaei, S.; Hedayati, M. The Influence of Embedded Plasmonic Nanostructures on the Optical Absorption of Perovskite Solar Cells. *Photonics* **2019**, *6*, 37. [[CrossRef](#)]
107. Dong, H.; Lei, T.; Yuan, F.; Xu, J.; Niu, Y.; Jiao, B.; Zhang, Z.; Ding, D.; Hou, X.; Wu, Z. Plasmonic enhancement for high efficient and stable perovskite solar cells by employing “hot spots” Au nanobipyramids. *Org. Electron.* **2018**, *60*, 1–8. [[CrossRef](#)]
108. Juan, F.; Wu, Y.; Shi, B.; Wang, M.; Wang, M.; Xu, F.; Jia, J.; Wei, H.; Yang, T.; Cao, B. Plasmonic Au Nanooctahedrons Enhance Light Harvesting and Photocarrier Extraction in Perovskite Solar Cell. *ACS Appl. Energy Mater.* **2021**, *4*, 3201–3209. [[CrossRef](#)]
109. Zhang, W.; Saliba, M.; Stranks, S.D.; Sun, Y.; Shi, X.; Wiesner, U.; Snaith, H.J. Enhancement of Perovskite-Based Solar Cells Employing Core–Shell Metal Nanoparticles. *Nano Lett.* **2013**, *13*, 4505–4510. [[CrossRef](#)] [[PubMed](#)]
110. Cui, X.; Chen, Y.; Zhang, M.; Harn, Y.W.; Qi, J.; Gao, L.; Wang, Z.L.; Huang, J.; Yang, Y.; Lin, Z. Tailoring carrier dynamics in perovskite solar cells via precise dimension and architecture control and interfacial positioning of plasmonic nanoparticles. *Energy Environ. Sci.* **2020**, *13*, 1743–1752. [[CrossRef](#)]
111. Qin, P.; Wu, T.; Wang, Z.; Xiao, L.; Ma, L.; Ye, F.; Xiong, L.; Chen, X.; Li, H.; Yu, X.; et al. Grain Boundary and Interface Passivation with Core–Shell Au@CdS Nanospheres for High-Efficiency Perovskite Solar Cells. *Adv. Funct. Mater.* **2020**, *30*, 1908408. [[CrossRef](#)]
112. Hao, H.; Wang, L.; Ma, X.; Cao, K.; Yu, H.; Wang, M.; Gu, W.; Zhu, R.; Anwar, M.S.; Chen, S.; et al. Improved efficiency of inverted Perovskite Solar Cells via surface plasmon resonance effect of Au@PSS core-shell tetrahedra nanoparticles. *Sol. Rrl* **2018**, *2*, 1800061. [[CrossRef](#)]
113. Wu, Y.; Sun, X.; Dai, S.; Li, M.; Zheng, L.; Wen, Q.; Tang, B.; Yun, D.-Q.; Xiao, L. Broad-Band-Enhanced Plasmonic Perovskite Solar Cells with Irregular Silver Nanomaterials. *ACS Appl. Mater. Interfaces* **2022**, *14*, 16269–16278. [[CrossRef](#)] [[PubMed](#)]
114. Zhang, L.; Jiang, H.; Huang, T.; Song, Y.; Wang, Y.; Wang, F.; Fan, L.; Liu, X.; Yang, L.; Liu, H. Ag-LSPR and molecular additive: A collaborative approach to improve the photovoltaic performance of perovskite solar cells. *Chem. Eng. J.* **2024**, *481*, 148572. [[CrossRef](#)]

115. Ma, X.; Ma, B.; Yu, T.; Xu, X.; Zhang, L.; Wang, W.; Cao, K.; Deng, L.; Chen, S.; Huang, W. In-depth Studies on Working Mechanism of Plasmon-Enhanced Inverted Perovskite Solar Cells Incorporated with Ag@SiO<sub>2</sub> Core-Shell Nanocubes. *ACS Appl. Energy Mater.* **2019**, *2*, 3605–3613. [[CrossRef](#)]
116. Yuan, M.; Liu, S.; Li, H.; Gao, Y.; Yu, S.; Yu, Y.; Meng, L.; Liu, W.; Zhang, J.; Gao, P. Perovskite-loaded plasmonic gold nanorod composites enhanced solar cell performance. *Adv. Compos. Hybrid Mater.* **2023**, *6*, 55. [[CrossRef](#)]
117. Lin, Y.-T.; Kumar, G.; Chen, F.-C. Interfacial plasmonic effects of gold nanoparticle-decorated graphene oxides on the performance of perovskite photovoltaic devices. *Sol. Energy* **2020**, *211*, 822–830. [[CrossRef](#)]
118. Liu, Z.; Li, Q.; Chen, K.; Cui, Y.; Intemann, J.J.; Leng, S.; Cui, M.; Qin, C.; Fei, L.; Yao, K.; et al. Tailoring carrier dynamics in inverted mesoporous perovskite solar cells with interface-engineered plasmonics. *J. Mater. Chem. A* **2021**, *9*, 2394–2403. [[CrossRef](#)]
119. Aeineh, N.; Barea, E.M.; Behjat, A.; Sharifi, N.; Mora-Seró, I. Inorganic Surface Engineering to Enhance Perovskite Solar Cell Efficiency. *ACS Appl. Mater. Interfaces* **2017**, *9*, 13181–13187. [[CrossRef](#)]
120. Luo, Q.; Zhang, C.; Deng, X.; Zhu, H.; Li, Z.; Wang, Z.; Chen, X.; Huang, S. Plasmonic Effects of Metallic Nanoparticles on Enhancing Performance of Perovskite Solar Cells. *ACS Appl. Mater. Interfaces* **2017**, *9*, 34821–34832. [[CrossRef](#)]
121. Ullah, I.; Hossain, M.A.; Armghan, A.; Rana, M.S.; Al Asad, M.A. The optoelectronic enhancement in perovskite solar cells using plasmonic metal-dielectric core-shell and nanorod nanoparticles. *Opt. Quantum Electron.* **2023**, *55*, 1018. [[CrossRef](#)]
122. Knight, M.W.; King, N.S.; Liu, L.; Everitt, H.O.; Nordlander, P.; Halas, N.J. Aluminum for Plasmonics. *ACS Nano* **2014**, *8*, 834–840. [[CrossRef](#)] [[PubMed](#)]
123. Knight, M.W.; Liu, L.; Wang, Y.; Brown, L.; Mukherjee, S.; King, N.S.; Everitt, H.O.; Nordlander, P.; Halas, N.J. Aluminum Plasmonic Nanoantennas. *Nano Lett.* **2012**, *12*, 6000–6004. [[CrossRef](#)] [[PubMed](#)]
124. Hylton, N.P.; Li, X.F.; Giannini, V.; Lee, K.H.; Ekins-Daukes, N.J.; Loo, J.; Vercauteren, D.; Van Dorpe, P.; Sodabanlu, H.; Sugiyama, M.; et al. Loss mitigation in plasmonic solar cells: Aluminium nanoparticles for broadband photocurrent enhancements in GaAs photodiodes. *Sci. Rep.* **2013**, *3*, 2874. [[CrossRef](#)] [[PubMed](#)]
125. Akimov, Y.A.; Koh, W.S. Design of Plasmonic Nanoparticles for Efficient Subwavelength Light Trapping in Thin-Film Solar Cells. *Plasmonics* **2010**, *6*, 155–161. [[CrossRef](#)]
126. Kesavan, A.V.; Rao, A.D.; Ramamurthy, P.C. Tailoring optoelectronic properties of CH<sub>3</sub>NH<sub>3</sub>PbI<sub>3</sub> perovskite photovoltaics using Al nanoparticle modified PC<sub>61</sub>BM layer. *Sol. Energy* **2020**, *201*, 621–627. [[CrossRef](#)]
127. Sahai, S.; Varshney, A. The Effect of Morphologies of Embedded Plasmonic Cu-nanoparticles on Solar Absorption of Perovskite Solar Cells. A Comprehensive Study. *Opt. Spectrosc.* **2021**, *129*, 1165–1172. [[CrossRef](#)]
128. Bao, Z.; Fu, N.; Qin, Y.; Lv, J.; Wang, Y.; He, J.; Hou, Y.; Jiao, C.; Chen, D.; Wu, Y.; et al. Broadband Plasmonic Enhancement of High-Efficiency Dye-Sensitized Solar Cells by Incorporating Au@Ag@SiO<sub>2</sub> Core-Shell Nanocuboids. *ACS Appl. Mater. Interfaces* **2019**, *12*, 538–545. [[CrossRef](#)]
129. Borah, R.; Verbruggen, S.W. Silver-Gold Bimetallic Alloy versus Core-Shell Nanoparticles: Implications for Plasmonic Enhancement and Photothermal Applications. *J. Phys. Chem. C* **2020**, *124*, 12081–12094. [[CrossRef](#)]
130. Pei, C.; Choi, M.S.; Yu, X.; Xue, H.; Xia, B.Y.; Park, H.S. Recent progress in emerging metal and covalent organic frameworks for electrochemical and functional capacitors. *J. Mater. Chem. A* **2021**, *9*, 8832–8869. [[CrossRef](#)]
131. Xie, W.; Zhou, J.; Huang, S.; Ou-Yang, W.; Xie, W.; Sun, Z.; Chen, X. Plasmon-enhanced perovskite solar cells using ultra-thin LiF spacer isolating AgAl and Au composite nanoparticles from metal electrode. *Org. Electron.* **2018**, *59*, 272–278. [[CrossRef](#)]
132. Fu, N.; Bao, Z.Y.; Zhang, Y.-L.; Zhang, G.; Ke, S.; Lin, P.; Dai, J.; Huang, H.; Lei, D.Y. Panchromatic thin perovskite solar cells with broadband plasmonic absorption enhancement and efficient light scattering management by Au@Ag core-shell nanocuboids. *Nano Energy* **2017**, *41*, 654–664. [[CrossRef](#)]
133. Lu, Z.; Pan, X.; Ma, Y.; Li, Y.; Zheng, L.; Zhang, D.; Xu, Q.; Chen, Z.; Wang, S.; Qu, B.; et al. Plasmonic-enhanced perovskite solar cells using alloy popcorn nanoparticles. *RSC Adv.* **2015**, *5*, 11175–11179. [[CrossRef](#)]
134. Sun, Z.; Xiahou, Y.; Cao, T.; Zhang, K.; Wang, Z.; Huang, P.; Zhu, K.; Yuan, L.; Zhou, Y.; Song, B.; et al. Enhanced p-i-n type perovskite solar cells by doping AuAg@AuAg core-shell alloy nanocrystals into PEDOT:PSS layer. *Org. Electron.* **2018**, *52*, 309–316. [[CrossRef](#)]
135. Han, N.; Ji, T.; Wang, W.; Li, G.; Li, Z.; Hao, Y.; Wu, Y.; Cui, Y. Boosting the efficiency of quasi two-dimensional perovskite solar cells via an interfacial layer of metallic nanoparticles. *Org. Electron.* **2019**, *74*, 190–196. [[CrossRef](#)]
136. Furasova, A.; Calabró, E.; Lamanna, E.; Tiguntseva, E.; Ushakova, E.; Ubyivovk, E.; Mikhailovskii, V.; Zakhidov, A.; Makarov, S.; Di Carlo, A. Resonant Silicon Nanoparticles for Enhanced Light Harvesting in Halide Perovskite Solar Cells. *Adv. Opt. Mater.* **2018**, *6*, 1800576. [[CrossRef](#)]
137. Deng, W.; Yuan, Z.; Liu, S.; Yang, Z.; Li, J.; Wang, E.; Wang, X.; Li, J. Plasmonic enhancement for high-efficiency planar heterojunction perovskite solar cells. *J. Power Sources* **2019**, *432*, 112–118. [[CrossRef](#)]
138. Yu, H.; Roh, J.; Yun, J.; Jang, J. Synergistic effects of three-dimensional orchid-like TiO<sub>2</sub> nanowire networks and plasmonic nanoparticles for highly efficient mesoscopic perovskite solar cells. *J. Mater. Chem. A* **2016**, *4*, 7322–7329. [[CrossRef](#)]
139. Zhang, C.; Luo, Q.; Shi, J.; Yue, L.; Wang, Z.; Chen, X.; Huang, S. Efficient perovskite solar cells by combination use of Au nanoparticles and insulating metal oxide. *Nanoscale* **2017**, *9*, 2852–2864. [[CrossRef](#)]
140. Cheng, Y.; Chen, C.; Chen, X.; Jin, J.; Li, H.; Song, H.; Dai, Q. Considerably enhanced perovskite solar cells via the introduction of metallic nanostructures. *J. Mater. Chem. A* **2017**, *5*, 6515–6521. [[CrossRef](#)]

141. Chen, X.; Gu, M. Hole Blocking Layer-Free Perovskite Solar Cells with High Efficiencies and Stabilities by Integrating Subwavelength-Sized Plasmonic Alloy Nanoparticles. *ACS Appl. Energy Mater.* **2019**, *2*, 2094–2103. [[CrossRef](#)]
142. Du, J.; Zhang, Y.; Yang, M.; Han, D.; Fan, L.; Sui, Y.; Yang, J.; Yang, L.; Wang, F. Hot-Carrier Injection Antennas with Hemispherical AgOx@Ag Architecture for Boosting the Efficiency of Perovskite Solar Cells. *ACS Appl. Mater. Interfaces* **2020**, *12*, 41446–41453. [[CrossRef](#)] [[PubMed](#)]
143. Yao, K.; Li, S.; Liu, Z.; Ying, Y.; Dvořák, P.; Fei, L.; Šikola, T.; Huang, H.; Nordlander, P.; Jen, A.K.Y.; et al. Plasmon-induced trap filling at grain boundaries in perovskite solar cells. *Light Sci. Appl.* **2021**, *10*, 219. [[CrossRef](#)] [[PubMed](#)]
144. Zarick, H.F.; Boulesbaa, A.; Poretzky, A.A.; Talbert, E.M.; DeBra, Z.R.; Soetan, N.; Geohegan, D.B.; Bardhan, R. Ultrafast carrier dynamics in bimetallic nanostructure-enhanced methylammonium lead bromide perovskites. *Nanoscale* **2017**, *9*, 1475–1483. [[CrossRef](#)] [[PubMed](#)]
145. Yin, J.; Qu, H.; Cao, J.; Tai, H.; Li, J.; Zheng, N. Light absorption enhancement by embedding submicron scattering TiO<sub>2</sub> nanoparticles in perovskite solar cells. *RSC Adv.* **2016**, *6*, 24596–24602. [[CrossRef](#)]
146. Mali, S.S.; Shim, C.S.; Kim, H.; Patil, P.S.; Hong, C.K. In situ processed gold nanoparticle-embedded TiO<sub>2</sub> nanofibers enabling plasmonic perovskite solar cells to exceed 14% conversion efficiency. *Nanoscale* **2016**, *8*, 2664–2677. [[CrossRef](#)]
147. Xia, Z.; Zhang, C.; Feng, Z.; Wu, Z.; Wang, Z.; Chen, X.; Huang, S. Synergetic Effect of Plasmonic Gold Nanorods and MgO for Perovskite Solar Cells. *Nanomaterials* **2020**, *10*, 1830. [[CrossRef](#)]
148. Zhang, C.; Li, Z.; Deng, X.; Yan, B.; Wang, Z.; Chen, X.; Sun, Z.; Huang, S. Enhancing photovoltaic performance of perovskite solar cells utilizing germanium nanoparticles. *Sol. Energy* **2019**, *188*, 839–848. [[CrossRef](#)]
149. Li, F.; Lo, T.W.; Deng, X.; Li, S.; Fan, Y.; Lin, F.R.; Cheng, Y.; Zhu, Z.; Lei, D.; Jen, A.K.Y. Plasmonic Local Heating Induced Strain Modulation for Enhanced Efficiency and Stability of Perovskite Solar Cells. *Adv. Energy Mater.* **2022**, *12*, 2200186. [[CrossRef](#)]
150. Liu, Y.; Lee, S.; Yin, Y.; Li, M.; Cotlet, M.; Nam, C.-Y.; Lee, J.-K. Near-Band-Edge Enhancement in Perovskite Solar Cells via Tunable Surface Plasmons. *Adv. Opt. Mater.* **2022**, *10*, 2201116. [[CrossRef](#)]
151. Omelianovych, O.; Sandhu, S.; Ewusi, M.A.; Larina, L.; Kim, B.; Trinh, B.T.; Szaniel, A.; Yoon, I.; Lee, J.J.; Choi, H.S. Stable and Efficient Perovskite Solar Cells by Controlling the Crystal Growth via Introduction of Plasmonic TiN Nanoparticles. *Adv. Funct. Mater.* **2024**, 2407343. [[CrossRef](#)]
152. Talebi, H.; Emami, F. Broadband plasmonic absorption enhancement of perovskite solar cells with embedded Au@SiO<sub>2</sub>@graphene core-shell nanoparticles. *Semicond. Sci. Technol.* **2022**, *37*, 055002. [[CrossRef](#)]
153. Taukeer Khan, M.; Khan, F. Enhancement in photovoltaic performance of perovskites solar cells through modifying the electron transport layer with reduced graphene oxide. *Mater. Lett.* **2022**, *323*, 132578. [[CrossRef](#)]
154. Oliveira, O.N.; Beljonne, D.; Wong, S.S.; Schanze, K.S. Forum on Artificial Intelligence/Machine Learning for Design and Development of Applied Materials. *ACS Appl. Mater. Interfaces* **2021**, *13*, 53301–53302. [[CrossRef](#)] [[PubMed](#)]
155. Fuhr, A.S.; Sumpter, B.G. Deep Generative Models for Materials Discovery and Machine Learning-Accelerated Innovation. *Front. Mater.* **2022**, *9*, 865270. [[CrossRef](#)]
156. Dean, J.; Scheffler, M.; Purcell, T.A.R.; Barabash, S.V.; Bhowmik, R.; Bazhurov, T. Interpretable machine learning for materials design. *J. Mater. Res.* **2023**, *38*, 4477–4496. [[CrossRef](#)]
157. Wang, J.; Xu, P.; Ji, X.; Li, M.; Lu, W. Feature Selection in Machine Learning for Perovskite Materials Design and Discovery. *Materials* **2023**, *16*, 3134. [[CrossRef](#)]
158. Thadson, K.; Sasivimolkul, S.; Suvarnaphaet, P.; Visitsattapongse, S.; Pechprasarn, S. Measurement precision enhancement of surface plasmon resonance based angular scanning detection using deep learning. *Sci. Rep.* **2022**, *12*, 2052. [[CrossRef](#)]

**Disclaimer/Publisher's Note:** The statements, opinions and data contained in all publications are solely those of the individual author(s) and contributor(s) and not of MDPI and/or the editor(s). MDPI and/or the editor(s) disclaim responsibility for any injury to people or property resulting from any ideas, methods, instructions or products referred to in the content.